Collective instabilities driven by anode plasma ions and electrons in a nonrelativistic cylindrical diode with applied magnetic field

Ronald C. Davidson

Plasma Fusion Center, Massachusetts Institute of Technology, Cambridge, Massachusetts 02139

Kang T. Tsang

Science Applications International Corporation, Boulder, Colorado 80302

Han S. Uhm

Naval Surface Weapons Center, Silver Spring, Maryland 20910
(Received 22 October 1984; revised manuscript received 15 March 1985)

Use is made of the macroscopic cold-fluid Poisson equations to investigate the electrostatic stability properties of nonrelativistic, non-neutral electron flow in a cylindrical diode with applied magnetic field $B_0\hat{e}_z$. The cathode is located at $r=a$ and the anode is located at $r=b$. Space-charge-limited flow with $E_r^0(r=a)=0$ is assumed. Detailed stability properties are investigated analytically and numerically for electrostatic flute perturbations with $\partial/\partial z=0$. Particular emphasis is placed on the influence of the neutral anode plasma on stability behavior assuming uniform cathode electron density ($\hat{n}_b$) extending from the cathode ($r=a$) to $r=r_b$, and uniform anode plasma density ($\hat{n}_e=Z_i\hat{n}_i$) extending from $r=r_p$ to the anode ($r=b$). Depending on the cathode electron density (as measured by $s_b=\hat{\omega}_{pb}^2/\omega_{ce}^2$), the anode plasma density (as measured by $s_e=\hat{\omega}_{pe}^2/\omega_{ce}^2$), the diode aspect ratio, etc., it is found that there can be a strong coupling of the anode plasma to the cathode electrons, and a concomitant large influence on detailed stability behavior for both the high-frequency (electron-driven) and low-frequency (ion-driven) branches. Detailed stability properties are investigated over a wide range of cathode electron density, anode plasma density, diode aspect ratio, etc.

I. INTRODUCTION AND SUMMARY

There is a growing literature on the equilibrium and linear stability properties of sheared, non-neutral electron flow in cylindrical[1] and planar[2-6] models of high-voltage diodes with application to the generation of intense charged-particle beams for inertial confinement fusion.[7] These analyses[1-6] have represented major extensions of earlier work[8-11] to include the important influence of cylindrical,[1] relativistic,[2-6] electromagnetic,[2-6] and kinetic[6] effects on stability behavior at moderately high electron density. However, none of these treatments[1-6] has included the influence of active plasma components in the anode-cathode gap. Indeed, it would be expected that plasma ions and electrons could interact effectively with the cathode electrons and modify stability behavior. For example, it is well established in applications related to heavy ion accelerators[12-14] and electron ring accelerators[15] and in basic theoretical studies[16-19] of non-neutral plasma stability properties that the collective interactions associated with an active ion component in an electron-rich background can lead to an instability known as the ion resonance instability.[12] The strength of the ion resonance instability depends on a number of factors, including ion density, the relative motion of electron and ion components, and the strength of the equilibrium self electric fields. As such an instability may have deleterious effects on stable diode operation and/or the production of well-collimated ion beams, one purpose of the present analysis is to investigate detailed properties of the ion resonance instability in geometry particular to cylindrical diodes (Fig. 1). In addition, we investigate the stability behavior associated with the (high-frequency) interaction of the plasma electrons with the cathode electrons.

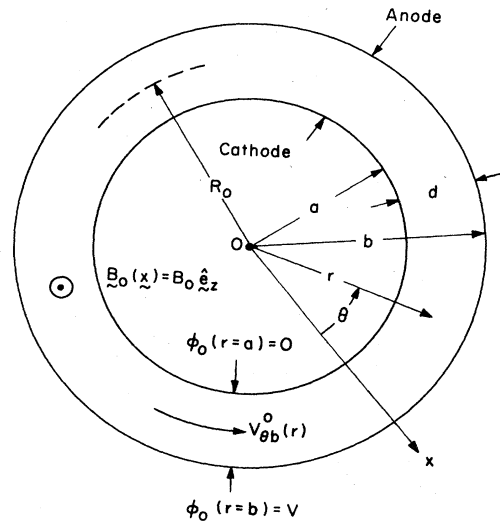In the present analysis, we make use of a macroscopic,

FIG. 1. Cylindrical diode configuration with cathode located at $r=a$ and anode at $r=b$. Equilibrium flow is in the θ direction, and the equilibrium space-charge density $\sum_j n_j^0(r)e_j$ produces a radial electric field $E_r^0(r)$ [Eq. (5)].

cold-fluid model to investigate the electrostatic equilibrium and stability properties of nonrelativistic non-neutral plasma in a cylindrical diode with applied magnetic field $B_0 \hat{e}_z$. As illustrated in Fig. 1, the cathode is located at $r = a$ and the anode at $r = b$, and space-charge-limited flow with $E_r^0(r = a) = 0$ is assumed. In general, the non-neutral plasma is assumed to consist of three components: electrons in the cathode region ($j = b$), positively charged ions ($j = i$), and plasma electrons ($j = e$). The macroscopic cold-fluid model used in the equilibrium (Sec. II) and stability (Secs. III—VI) analysis is based on the continuity and momentum transfer equations for the density $n_j(\mathbf{x}, t)$ and mean velocity $\mathbf{V}_j(\mathbf{x}, t)$. Moreover, the electric field $\mathbf{E}(\mathbf{x}, t) = -\nabla\phi(\mathbf{x}, t)$ is determined self-consistently from Poisson's equation, and $\partial/\partial z = 0$ is assumed for both equilibrium and perturbed quantities.

Under steady-state conditions ($\partial/\partial t = 0$), the equilibrium analysis (Sec. II) allows for general density profiles $n_j^0(r)$ ($j = b, e, i$) and corresponding self-consistent radial electric field [Eq. (5)]

$$E_r^0 = \sum_j 4\pi e_j \frac{1}{r} \int_a^r dr' r' n_j^0(r') \ .$$

Moreover, equilibrium force balance in the radial direction [Eqs. (8) and (11)] can be used to determine the angular rotation velocity $\omega_{rj}(r) = V_{\theta j}^0(r)/r$ of the jth component fluid element. For slow rotational equilibria satisfying $\omega_{rj}^-(r = a) = 0$, the rotation velocities are given by [Eqs. (13) and (14)]

$$\omega_{rj}^-(r) = \tfrac{1}{2}\{\omega_{ce} - [\omega_{ce}^2 - 4\omega_{ce}\omega_E(r)]^{1/2}\}, \quad j = b, e$$

$$\omega_{rj}^-(r) = \tfrac{1}{2}\{-\omega_{ci} + [\omega_{ci}^2 + 4\omega_{ci}\omega_E(r)]^{1/2}\}, \quad j = i$$

in the regions where $n_j^0(r)$ is nonzero. Here, $\omega_E(r) = -cE_r^0/rB_0$ is the $\mathbf{E}^0 \times B_0\hat{e}_z$ rotation frequency, $\omega_{ce} = eB_0/m_e c$ and $\omega_{ci} = Z_i eB_0/m_i c$ are the cyclotron frequencies, and Z_i is the degree of ionization of the ions. As specific examples, detailed equilibrium properties are investigated for two cases: a neutral plasma in the anode region (Sec. II B and Fig. 2), and ion-contaminated cathode electrons (Sec. II C and Fig. 4).

Stability properties are investigated in Sec. III for small-amplitude electrostatic perturbations about general equilibrium profiles $n_j^0(r)$, $E_r^0(r)$, and $\omega_{rj}^-(r)$. Expressing $\delta\phi(r, \theta, t) = \sum_l \delta\phi^l(r) \exp(il\theta - i\omega t)$, where $\mathrm{Im}\,\omega > 0$ corresponds to instability, the linearized cold-fluid Poisson equations give the eigenvalue equation for $\delta\phi^l(r)$ [Eq. (42)][20]

$$\frac{1}{r}\frac{\partial}{\partial r}\left[r\left(1 + \sum_j \chi_j\right)\frac{\partial}{\partial r}\delta\phi^l\right] - \frac{l^2}{r^2}\left(1 + \sum_j \chi_j\right)\delta\phi^l$$

$$= -\frac{l\,\delta\phi^l}{r}\sum_j \frac{1}{\omega - l\omega_{rj}^-}\frac{\partial}{\partial r}\left[\frac{\omega_{pj}^2(\epsilon_j \omega_{cj} + \omega_{rj}^-)}{v_j^2}\right],$$

where $\omega_{pj}^2(r) = 4\pi n_j^0(r) e_j^2/m_j$, $\epsilon_j = \mathrm{sgn}\,e_j$, the effective susceptibility $\chi_j(r, \omega)$ is defined by [Eq. (43)]

$$\chi_j(r, \omega) = -\frac{\omega_{pj}^2(r)}{v_j^2(r, \omega)} \ ,$$

and $v_j^2(r, \omega)$ is defined by [Eq. (47)]

$$v_j^2(r, \omega) = (\omega - l\omega_{rj}^-)^2 - \left[\omega_{cj}^2 + 2\epsilon_j \omega_{cj}\omega_E(r) - \frac{4\pi e_j}{m_j}\sum_k e_k n_k^0(r)\right].$$

The summations $\sum_j$ and $\sum_k$ are over all plasma components (b, e, i), and Eq. (42) is to be solved subject to the boundary conditions $\delta\phi^l(r = a) = 0 = \delta\phi^l(r = b)$. The exact eigenvalue equation (42) is simplified in Sec. III B for the special case of rectangular density profiles for the cathode electrons and for the neutral plasma ions and electrons in the anode region (Fig. 2). The resulting eigenvalue equation (48), together with the definitions in Eqs. (19)—(21) and (49)—(54), have a wide range of applicability and are analyzed numerically in Sec. VI. That is, in Eqs. (48)—(54), there is no a priori assumption that the diode aspect ratio is large, that the density is low, etc.

As an example that is analytically tractable, in Sec. IV (see also Fig. 5) we simplify the eigenvalue equation (48) in circumstances where the anode plasma density is low [Eq. (55)], the cathode electrons are strongly magnetized [Eq. (56)], the diode aspect ratio is large [Eq. (57)], the perturbation frequency is low [Eq. (58)], and the anode plasma is in contact with the cathode electrons [Eq. (59)]. This gives the approximate eigenvalue equation [Eq. (66)]

$$\frac{1}{r}\frac{\partial}{\partial r}\left[r(1 + \chi_i)\frac{\partial}{\partial r}\delta\phi^l\right] - \frac{l^2}{r^2}(1 + \chi_i)\delta\phi^l$$

$$= \frac{l\,\delta\phi^l}{r}\frac{(\hat{\omega}_{pb}^2/\omega_{ce})}{\omega - l\omega_E(r)}\delta(r - r_b) \ ,$$

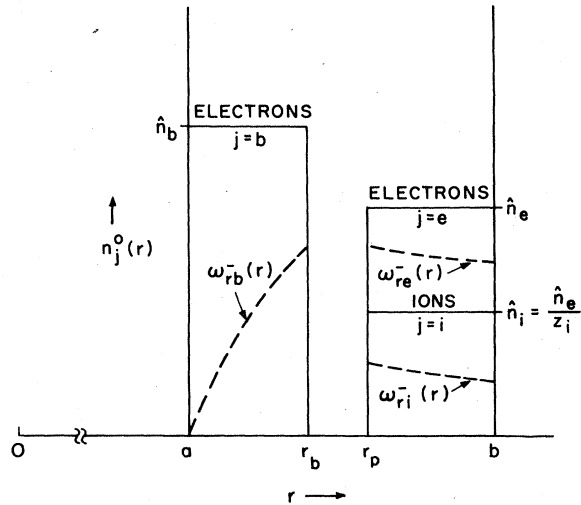where $\chi_i(r, \omega)$ is defined by [Eq. (64)]

FIG. 2. Plots of equilibrium density $n_j^0(r)$ and angular velocity $\omega_{rj}^-(r)$ vs r obtained from Eqs. (15)—(17) and (19)—(21). Electrons in the cathode region have a rectangular density profile extending from $r = a$ to $r = r_b$. The plasma in the anode region is electrically neutral with $Z_i n_i^0(r) = n_e^0(r)$, and extends from $r = r_p$ to $r = b$.

$$\chi_i(r,\omega)=\begin{cases}0, & a<r<r_b \\ -\dfrac{\hat{\omega}_{pi}^2}{(\omega-l\hat{\omega}_{ri}^-)^2-(\omega_{ci}^2+2\omega_{ci}\hat{\Omega}_E)}, & r_b<r<b .\end{cases}$$

Here, $\hat{\Omega}_E=\omega_E(r_b)=(\hat{\omega}_{pb}^2/\omega_{ce})(r_b-a)/r_b$ [Eqs. (60) and (62)], $\hat{\omega}_{pi}^2=4\pi\hat{n}_iZ_i^2e^2/m_i$, $\hat{\omega}_{pb}^2=4\pi\hat{n}_be^2/m_e$, and $\hat{\omega}_{ri}^-=\frac{1}{2}[-\omega_{ci}+(\omega_{ci}^2+4\omega_{ci}\hat{\Omega}_E)^{1/2}]$ [Eq. (61)]. It is clear from Eq. (66) that the surface-charge perturbation on the cathode electron layer can couple to the dielectric response of the plasma ions in the anode region. Solving Eq. (66) for a large-aspect-ratio diode with $(b-a)/a\ll1$ gives the approximate dispersion relation [Eq. (75)]

$$\left[1+\frac{\Delta_p}{\Delta_b}\right]-\frac{\hat{\omega}_{pi}^2}{(\omega-l\hat{\omega}_{ri}^-)^2-(\omega_{ci}^2+2\omega_{ci}\hat{\Omega}_E)}$$
$$=-\frac{\Delta_p}{\Delta_b}\frac{l\hat{\Omega}_E}{\omega-l\hat{\Omega}_E},$$

where $\Delta_b=r_b-a$ and $\Delta_p=b-r_b$ (Fig. 5), and $\Delta_b,\Delta_p\ll r_b$ is assumed. The dispersion relation (75) is analyzed in Sec. IV and stability properties are investigated over a wide range of the dimensionless parameters $\omega_{ci}/\hat{\Omega}_E=(Z_im_e/m_i)(\omega_{ce}^2/\hat{\omega}_{pb}^2)(r_b/\Delta_b)$ and $\hat{\omega}_{pi}^2/\hat{\Omega}_E^2=(Z_i\hat{n}_i/\hat{n}_b)(r_b/\Delta_b)(\omega_{ci}/\hat{\Omega}_E)$. A strong variant of the ion resonance instability[12] is found for a wide range of system parameters. Although the assumptions in Sec. IV are somewhat restrictive, the analysis clearly establishes the existence and qualitative features of the ion resonance instability and the fact that the plasma ions in the anode region can strongly couple to the cathode electrons.

As a second example that is analytically tractable, in Sec. V we investigate the eigenvalue equation (48) in circumstances where the anode plasma is not in contact with the cathode electrons [Fig. 2 and Eq. (81)]. Assuming high-frequency perturbations [Eq. (83)], unmagnetized ions [Eqs. (82) and (84)], and low-density electrons [Eq. (85)], it is found that the cathode electrons and anode plasma electrons combine to give the diocotron instability driven by electron velocity shear over the interval $a<r<b$. For infinitely massive ions, the resulting approximate eigenvalue equation (86) is solved exactly to give the dispersion relation [Eq. (93)]

$$\left[1-\left[\frac{b}{r_p}\right]^{2l}\right]\left[1+\frac{1-(a/r_b)^{2l}}{\omega/\omega_D-l(r_b^2-a^2)/r_b^2}\right]$$
$$=\left[1+\frac{(\hat{n}_e/\hat{n}_b)[1-(b/r_p)^{2l}]}{\omega/\omega_D-l(r_b^2-a^2)/r_p^2}\right]$$
$$\times\left[1-\left[\frac{a}{r_p}\right]^{2l}\right]$$
$$+\left[1-\frac{r_b^{2l}}{r_p^{2l}}\right]\frac{1-(a/r_b)^{2l}}{\omega/\omega_D-l(r_b^2-a^2)/r_b^2}\right],$$

which determines the complex oscillation frequency ω in terms of geometric factors, the density ratio $\hat{n}_e/\hat{n}_b$, and the diocotron frequency $\omega_D=\hat{\omega}_{pb}^2/2\omega_{ce}$. In Sec. V, the dispersion relation (93) is used to investigate detailed sta-

bility properties over a wide range of system parameters $\hat{n}_e/\hat{n}_b$, r_p/a, r_b/a, and harmonic number l. In the unstable region of parameter space, it is found that the instability growth rate can be substantial (in the range of $0.1\omega_D$), even within the context of the low-density assumption made in Sec. V [Eq. (85)].

In Sec. VI, we make use of the exact eigenvalue equation (48) to investigate numerically electrostatic stability properties for the choice of rectangular density profiles illustrated in Fig. 2. The anode plasma is assumed to be electrically neutral hydrogen plasma ($\hat{n}_e=\hat{n}_i$). No a priori assumption is made that the cathode electron density (as measured by $s_b=\hat{\omega}_{pb}^2/\omega_{ce}^2$) or the anode plasma density (as measured by $s_e=\hat{\omega}_{pe}^2/\omega_{ce}^2$) is small. In the absence of anode plasma ($s_e=0$), the conventional diocotron instability[1] driven by the cathode electrons is recovered. At low cathode electron density, this instability is extremely weak [$(\mathrm{Im}\omega)/\omega_{ce}<10^{-4}$ for $s_b=0.1$ and $s_e=0$], although the growth rate does become substantial as s_b is increased to larger values. In the presence of anode plasma ($s_e\neq0$), the numerical analysis in Sec. VI shows that both the anode plasma ions and the anode plasma electrons can have a large influence on stability behavior, even at low density. Indeed, the presence of the anode plasma introduces a new low-frequency mode (ion resonance instability) in which there is a strong coupling between the cathode electrons and the anode plasma ions. Moreover, the conventional high-frequency stability properties calculated for $s_e=0$ are significantly modified by the coupling between the cathode electrons and the anode plasma electrons. For example, for the parameters chosen in Fig. 12(b), it is found that $(\mathrm{Im}\omega)/\omega_{ce}=3.5\times10^{-4}$ for $s_e=0$ and $s_b=0.2$, whereas $(\mathrm{Im}\omega)/\omega_{ce}=10^{-2}$ for $s_e=0.1$ and $s_b=0.2$. In Sec. VI, the numerical studies of detailed stability properties are carried out for a wide range of system parameters s_b, s_e, diode aspect ratio, etc.

Finally, it is important to note that inclusion of the effects of finite resistivity of the anode or cathode plasma can also have an important influence on stability properties, particularly for low-frequency perturbations.[21,22] We refer here to the recent investigations by Chang et al.[21] and Desjarlais and Sudan[22] who assume a thin ($\delta\ll b-a$) resistive plasma layer with current $\mathbf{J}_p=\vec{\sigma}\cdot\delta\mathbf{E}$ adjacent to the cathode,[21] or to both electrodes.[22] Here, $\vec{\sigma}$ is the conductivity tensor, and the electron-ion collision frequency ν is assumed to satisfy[21] $\nu\gg|\omega|$, $\nu\gg\omega_{pe}^2/|\omega|$, and $\nu^2\geq\omega_{ce}^2$. The sheath electrons (treated as a relativistic, collisionless, cold fluid in Refs. 21 and 22) interact with the resistive electrode plasma. One of the most important consequences of finite plasma resistivity[21] is the appearance of a resistivity-driven unstable mode in which the growth rate exhibits a pronounced peak at the zero frequency of the slow-mode branch, which separates the regions of positive and negative wave energy. In terms of sheath thickness (δ) and conductivity ($\sigma\sim\omega_{pe}^2/4\pi\nu$), the characteristic maximum growth rate of this low-frequency instability[21] scales as $(\delta/\sigma)^{1/2}\sim(\delta\nu)^{1/2}$.

Depending on the parameter regime, it is evident that the effects of finite plasma resistivity can play an important role,[21,22] particularly for low-frequency perturbations and a collisional electrode plasma. In this regard, we wish

to emphasize some of the features of the present analysis and model that are complementary to the work[21,22] described in the preceding paragraph.

First, the present analysis is electrostatic, and treats the sheath electrons nonrelativistically in cylindrical geometry. On the other hand, the analysis in Refs. 21 and 22 is fully electromagnetic and treats the sheath electrons relativistically in planar geometry. While the range of applicability of the present electrostatic, nonrelativistic model is necessarily restricted to low values of applied diode voltage V_s, the analysis does incorporate cylindrical effects and the influence of finite aspect ratio of the diode in a fully self-consistent manner. Indeed, it is found (Sec. IV—VI) that the instability growth rate and real oscillation frequency of the modes considered here exhibit a strong dependence on diode aspect ratio. In addition, no *a priori* assumption is made in the present analysis that the electrode plasma layer is thin ($\delta \ll b - a$).

Second, the present analysis treats the electrode plasma as collisionless ($\nu \rightarrow 0$), and describes the collective interaction of the plasma electrons and ions with the cathode electrons. That is, the present analysis assumes perturbations with sufficiently high frequency that

$$|\omega| \gg \nu ,$$

and the plasma electrons and ions are treated as active components interacting with the applied and collective fields. The assumption that $|\omega| \gg \nu$ is the most important aspect in which the present analysis complements the work in Ref. 21 and 22 (which assume $|\omega| \ll \nu$). This requires perturbations with much higher frequency and/or a sufficiently "warm" electrode plasma that the collision frequency is much lower. In this regard, at moderate values of $\omega_{pb}^2/\omega_{ce}^2$, it is evident from the analysis in Sec. VI (e.g., see Figs. 13 and 14) that even the "low-frequency" (ion resonance) branch has a relatively high frequency, which must exceed the collision frequency ν for the present analysis to be valid.

Third, the present model treats the collisionless dynamics of the plasma electrons and ions in a self-consistent manner, retaining both electron and ion inertial effects. In the parameter regime considered here, these effects have an important influence on stability behavior. Indeed, the ion resonance instability is associated with the active interaction of the plasma ions with the collective fields of the sheath electrons. This is in contrast with the resistive model used in Refs. 21 and 22, where the active ion dynamics are neglected and the plasma current $\mathbf{J}_p = \overleftrightarrow{\sigma} \cdot \delta \mathbf{E}$ is carried by the plasma electrons colliding with the background ions.

To summarize, it is evident that the present analysis complements the work in Refs. 21 and 22. Moreover, it is important to keep in mind the different ranges of validity of the two models. For example, to investigate the detailed features of instabilities driven by collisionless anode plasma in a high-voltage diode, it is necessary to extend the present analysis to include both electromagnetic effects and relativistic electron dynamics. In contrast, electromagnetic effects and the relativistic dynamics of the sheath electrons are incorporated in the analyses in Refs. 21 and 22.

II. COLD-FLUID EQUILIBRIUM FOR A CYLINDRICAL DIODE

A. Equilibrium model and assumptions

We consider here the steady-state equilibrium properties ($\partial/\partial t = 0$) of a cold, non-neutral plasma[11] confined in the cylindrical diode configuration illustrated in Fig. 1. The non-neutral plasma is generally assumed to consist of three components: cathode electrons ($j = b$), positively charged ions ($j = i$), and plasma electrons ($j = e$). The plasma electrons may overlap spatially with the ions, e.g., for the case of a neutral plasma in the vicinity of the anode (Fig. 2). As illustrated in Fig. 1, the cathode is located at $r = a$ and the anode at $r = b$, where $d = b - a$ is the anode-cathode spacing. Moreover, the non-neutral plasma is immersed in a uniform applied magnetic field

$$\mathbf{B}_0 = B_0 \hat{\mathbf{e}}_z . \tag{1}$$

For simplicity, the present analysis is based on a nonrelativistic, electrostatic, cold-fluid model for each plasma component ($j = b, e, i$). In equilibrium ($\partial/\partial t = 0$), the following simplifying assumptions are also made.

(a) All equilibrium properties are uniform in the z direction ($\partial/\partial z = 0$), and there is no equilibrium electric field parallel to $B_0 \hat{\mathbf{e}}_z$, i.e., $\mathbf{E}^0(\mathbf{x}) \cdot \hat{\mathbf{e}}_z = 0$. All equilibrium properties are assumed to be azimuthally symmetric ($\partial/\partial\theta = 0$) about the diode axis, e.g., the equilibrium density and azimuthal flow velocity components satisfy

$$n_j^0(\mathbf{x}) = n_j^0(r) ,$$
$$\mathbf{V}_j^0(\mathbf{x}) = V_{\theta j}^0(r) \hat{\mathbf{e}}_\theta , \tag{2}$$

where $\hat{\mathbf{e}}_\theta$ is a unit vector in the θ direction, and $r = (x^2 + y^2)^{1/2}$ is the radial distance from the axis of symmetry.

(b) Equilibrium diamagnetic effects are assumed to be negligibly small in comparison with the applied magnetic field $B_0 \hat{\mathbf{e}}_z$. That is, the equilibrium azimuthal current $\sum_j n_j^0(r) e_j V_{\theta j}^0(r)$ generally produces an axial self magnetic field $B_z^s(r)$. The present analysis assumes that $|B_z^s(r)| \ll B_0$.

(c) In general, the plasma is electrically non-neutral and there is a corresponding equilibrium radial electric field

$$\mathbf{E}_0(\mathbf{x}) = E_r^0(r) \hat{\mathbf{e}}_r , \tag{3}$$

where $E_r^0(r)$ is determined self-consistently from the steady-state Poisson equation

$$\frac{1}{r} \frac{\partial}{\partial r} [r E_r^0(r)] = \sum_j 4\pi e_j n_j^0(r) . \tag{4}$$

Here, the summation is over $j = b, e, i$, where $e_j = -e$ for the cathode electrons ($j = b$) and plasma electrons ($j = e$). Moreover, $e_i = +Z_i e$ for the positive ions, where Z_i is the degree of ionization.

(d) Space-charge-limited flow with $E_r^0(r = a) = 0$ is assumed. Integrating Eq. (4) then gives for $E_r^0(r)$

$$E_r^0(r) = \sum_j 4\pi e_j \frac{1}{r} \int_a^r dr' r' n_j^0(r') . \tag{5}$$

Expressing $E_r^0 = -\partial\phi^0/\partial r$, where $\phi^0(r)$ is the equilibrium electrostatic potential, we impose the boundary conditions

$$\phi_0(r=a)=0 ,$$

$$\phi_0(r=b)=V_s ,$$

(6)

where the anode voltage V_s consistent with Eq. (5) and $E_r^0(r=a)=0$ is given by

$$V_s = \phi_0(b) = -\sum_j 4\pi e_j \int_a^r \frac{dr''}{r''} \int_a^{r''} dr' r' n_j^0(r') . \quad (7)$$

(e) Finally, within the context of the present nonrelativistic, cold-fluid model, equilibrium radial force balance on the jth component fluid element can be expressed as

$$-\frac{m_j(V_{\theta j}^0)^2}{r} = e_j \left[E_r^0(r) + \frac{1}{c} V_{\theta j}^0(r) B_0 \right] , \quad (8)$$

corresponding to a balance of centrifugal, electric, and magnetic forces in the region where $n_j^0(r)$ is nonzero.

In the subsequent analysis, it is convenient to introduce the equilibrium angular rotation velocity $\omega_{rj}(r)$ defined by

$$V_{\theta j}^0(r) = \omega_{rj}(r)r , \quad (9)$$

and the $\mathbf{E}^0 \times B_0 \hat{\mathbf{e}}_z$ rotation frequency $\omega_E(r)$ defined by

$$\omega_E(r) = -\frac{cE_r^0(r)}{rB_0} = -\sum_j \frac{4\pi e_j c}{B_0 r^2} \int_a^r dr' r' n_j^0(r') . \quad (10)$$

Making use of Eqs. (9) and (10), the equilibrium force balance equation (8) can be expressed as

$$\omega_{rj}^2(r) + \epsilon_j \omega_{cj} \omega_{rj}(r) - \epsilon_j \omega_{cj} \omega_E(r) = 0 , \quad (11)$$

where

$$\omega_{cj} = \frac{|e_j| B_0}{m_j c} , \quad \epsilon_j = \mathrm{sgn} e_j . \quad (12)$$

Equation (11) generally supports two solutions for ω_{rj}, corresponding to fast (ω_{rj}^+) and slow (ω_{rj}^-) rotational equilibria. For present purposes, we consider *slow* rotational equilibria satisfying $\omega_{rj}^-(r=a)=0$. Therefore, in the regions where $n_j^0(r)$ is nonzero, Eq. (11) gives

$$\omega_{rj} \equiv \omega_{rj}^-(r) = \frac{1}{2}\{\omega_{ce} - [\omega_{ce}^2 - 4\omega_{ce}\omega_E(r)]^{1/2}\}, \quad j=b,e$$

(13)

for the cathode and plasma electrons, and

$$\omega_{ri} \equiv \omega_{ri}^-(r) = \frac{1}{2}\{-\omega_{ci} + [\omega_{ci}^2 + 4\omega_{ci}\omega_E(r)]^{1/2}\}, \quad j=i$$

(14)

for the plasma ions. Here, $\omega_E(r)$ is defined in Eq. (10), and $\omega_{ce} = eB_0/m_e c$ and $\omega_{ci} = Z_i eB_0/m_i c$ are the cyclotron frequencies.

B. Neutral anode plasma

As a first equilibrium example, we consider the case illustrated in Fig. 2. The cathode electrons $(j=b)$ are assumed to have the rectangular density profile

$$n_b^0(r) = \begin{cases} \hat{n}_b = \text{const}, & a < r < r_b \\ 0, & r_b < r < b . \end{cases} \quad (15)$$

Moreover, there is a neutral plasma in the vicinity of the anode with ion density profile

$$n_i^0(r) = \begin{cases} 0, & a < r < r_p \\ \hat{n}_i = \text{const}, & r_p < r < b . \end{cases} \quad (16)$$

The electrons are assumed to provide complete charge neutralization in the region $r_p < r < b$ with

$$n_e^0(r) = Z_i n_i^0(r) . \quad (17)$$

Making use of Eqs. (15)–(17), Poisson's equation (4) can be integrated to give

$$E_r^0 = \begin{cases} \dfrac{-2\pi \hat{n}_b e}{r}(r^2 - a^2), & a < r < r_b \\ \dfrac{-2\pi \hat{n}_b e}{r}(r_b^2 - a^2), & r_b < r < b . \end{cases} \quad (18)$$

Defining $\hat{\omega}_{pb}^2 = 4\pi \hat{n}_b e^2/m_e$, and making use of $\omega_E(r) = -cE_r^0/rB_0$, Eqs. (13) and (18) give for the electrons in the cathode region

$$\omega_{rb}^-(r) = \frac{1}{2}\left\{\omega_{ce} - \left[\omega_{ce}^2 - 2\hat{\omega}_{pb}^2 \left[\frac{r^2 - a^2}{r^2}\right]\right]^{1/2}\right\},$$

$$a < r < r_b . \quad (19)$$

On the other hand, from Eqs. (13) and (18), the plasma electrons in the anode region have equilibrium rotation velocity

$$\omega_{re}^-(r) = \frac{1}{2}\left\{\omega_{ce} - \left[\omega_{ce}^2 - 2\hat{\omega}_{pb}^2 \left[\frac{r_b^2 - a^2}{r^2}\right]\right]^{1/2}\right\},$$

$$r_p < r < b \quad (20)$$

and from Eqs. (14) and (18), $\omega_{ri}^-(r)$ is given by

$$\omega_{ri}^-(r) = \frac{1}{2}\left\{-\omega_{ci} + \left[\omega_{ci}^2 + 2\frac{Z_i m_e}{m_i}\hat{\omega}_{pb}^2 \left[\frac{r_b^2 - a^2}{r^2}\right]\right]^{1/2}\right\},$$

$$r_p < r < b \quad (21)$$

for the plasma ions in the anode region. The rotation velocities $\omega_{rj}(r)$ $(j=b,e,i)$ are illustrated schematically in Fig. 2.

It is convenient to introduce (for $a < r < r_b$)

$$\omega_E(r) = \frac{\hat{\omega}_{pb}^2}{2\omega_{ce}} \left[\frac{r^2 - a^2}{r^2}\right] \quad (22)$$

in Eq. (19). For

$$\frac{2\hat{\omega}_{pb}^2}{\omega_{ce}^2} \left[\frac{r_b^2 - a^2}{r_b^2}\right] \ll 1 , \quad (23)$$

it is clear from Eq. (19) that ω_{rb}^- can be approximated by

$$\omega_{rb}^-(r) = \omega_E(r), \quad a < r < r_b \tag{24}$$

where $\omega_E(r)$ is defined in Eq. (22). For a large-aspect-ratio diode with $(r_b^2 - a^2)/r_b^2 \ll 1$, note that Eq. (23) is easily satisfied even at moderately high electron densities with $2\hat{\omega}_{pb}^2 \lesssim \omega_{ce}^2$. Making use of Eq. (23), the angular velocity of the plasma electrons is given by the approximate expression

$$\omega_{re}^-(r) = \hat{\Omega}_E \frac{r_b^2}{r^2}, \quad r_p < r < b \tag{25}$$

where

$$\hat{\Omega}_E \equiv \omega_E(r_b) = \frac{\hat{\omega}_{pb}^2}{2\omega_{ce}} \left[\frac{r_b^2 - a^2}{r_b^2} \right]. \tag{26}$$

Moreover, Eq. (21) can be expressed as

$$\omega_{ri}^-(r) = \frac{1}{2} \left[-\omega_{ci} + \left[\omega_{ci}^2 + 4\omega_{ci}\hat{\Omega}_E \frac{r_b^2}{r^2} \right]^{1/2} \right],$$
$$r_p < r < b. \tag{27}$$

For strongly magnetized ions with $\hat{\Omega}_E \ll \omega_{ci}/4$, Eq. (27) reduces to the $\mathbf{E}^0 \times \mathbf{B}_0$ rotation frequency

$$\omega_{ri}^-(r) = \hat{\Omega}_E \frac{r_b^2}{r^2}, \quad r_p < r < b. \tag{28}$$

On the other hand, for weakly magnetized ions with $\hat{\Omega}_E \gg \omega_{ci}/4$, Eq. (27) reduces to

$$\omega_{ri}^-(r) = (\omega_{ci}\hat{\Omega}_E)^{1/2} \frac{r_b}{r}, \quad r_p < r < b. \tag{29}$$

In both cases, for a diode with moderately large aspect ratio, $(b-a)^2/a^2 \ll 1$, Eqs. (27)–(29) exhibit only a weak variation of $\omega_{ri}^-(r)$ with r over the anode plasma region ($r_p < r < b$).

Figure 3 shows a plot of ω_{ri}^- versus $\hat{\Omega}_E/\omega_{ci}$ for the case $r_p = r_b$ and $r = r_b$. Note from Eq. (26) that $\hat{\Omega}_E/\omega_{ci}$ is related to other equilibrium parameters by

$$\frac{\hat{\Omega}_E}{\omega_{ci}} = \frac{m_i}{Z_i m_e} \frac{\hat{\omega}_{pb}^2}{2\omega_{ce}^2} \left[\frac{r_b^2 - a^2}{r_b^2} \right]. \tag{30}$$
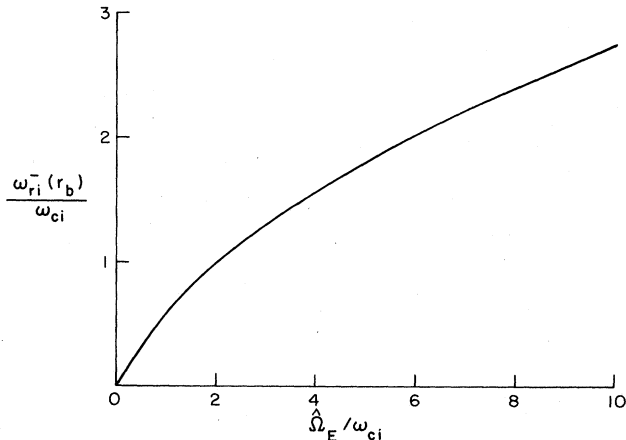
FIG. 3. Plot of $\omega_{ri}^-(r_b)$ vs $\hat{\Omega}_E/\omega_{ci} = (m_i/Z_i m_e)(\hat{\omega}_{pb}^2/2\omega_{ce}^2)[(r_b^2 - a^2)/r_b^2]$ obtained from Eq. (27) for $r_p = r_b$ and $r = r_b$.

Therefore, the region $\hat{\Omega}_E/\omega_{ci} \gg 1$ in Fig. 3 corresponds to sufficiently high density of the cathode electrons that the inequality

$$\frac{\hat{\omega}_{pb}^2}{2\omega_{ce}^2} \left[\frac{r_b^2 - a^2}{r_b^2} \right] \gg \frac{Z_i m_e}{m_i} \tag{31}$$

is satisfied.

C. Ion-contaminated cathode electrons

As a second equilibrium example, we consider the case illustrated in Fig. 4 where the cathode electrons are partially neutralized by a positive ion background.[12] In particular, it is assumed that $n_b^0(r)$ has the rectangular profile

$$n_b^0(r) = \begin{cases} \hat{n}_b = \text{const}, & a < r < r_b \\ 0, & r_b < r < b \end{cases} \tag{32}$$

and that the ion density profile $n_i^0(r)$ is related to $n_b^0(r)$ by

$$Z_i n_i^0(r) = f n_b^0(r), \tag{33}$$

where $f = \text{const}$ is the fractional charge neutralization. There is not a second component of electrons in the present equilibrium example, i.e., $n_e^0(r) = 0$. Making use of Eqs. (32) and (33), we determine $E_r^0(r)$ from Eq. (5). This gives

$$E_r^0 = \begin{cases} \dfrac{-2\pi e \hat{n}_b(1-f)}{r}(r^2 - a^2), & a < r < r_b \\ \dfrac{-2\pi e \hat{n}_b(1-f)}{r}(r_b^2 - a^2), & r_b < r < b. \end{cases} \tag{34}$$

Therefore, from Eq. (10), $\omega_E(r)$ is given by

$$\omega_E(r) = \frac{\hat{\omega}_{pb}^2}{2\omega_{ce}}(1-f)\frac{r^2 - a^2}{r^2} \tag{35}$$
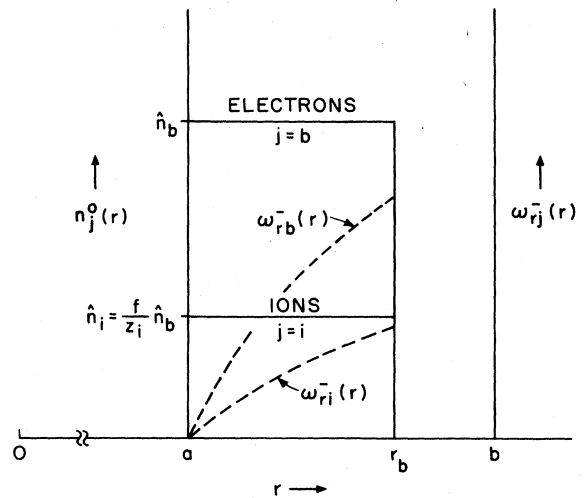

FIG. 4. Plots of equilibrium density $n_j^0(r)$ and angular velocity $\omega_{rj}^-(r)$ vs r obtained from Eqs. (32) and (33) and Eqs. (36) and (37). The cathode electrons are partially charge neutralized by positive ions with $Z_i n_i^0(r) = f n_b^0(r)$, where the fractional charge neutralization $f = \text{const}$.

over the interval $a < r < r_b$. For $\omega_E(r) \ll \omega_{ce}/4$, it follows from Eq. (13) that the angular rotation velocity of the cathode electrons can be approximated by

$$\omega_{rb}^-(r) = \omega_E(r), \quad a < r < r_b \tag{36}$$

where $\omega_E(r)$ is defined in Eq. (35). Finally, defining $\hat{\Omega}_E \equiv \omega_E(r_b) = (\hat{\omega}_{pb}^2/2\omega_{ce})(1-f)(r_b^2-a^2)/r_b^2$, and making use of Eqs. (14) and (35), the ion rotation velocity can be expressed as

$$\omega_{ri}^-(r) = \frac{1}{2}\left[-\omega_{ci} + \left[\omega_{ci}^2 + 4\omega_{ci}\hat{\Omega}_E \frac{r_b^2}{r^2}\frac{r^2-a^2}{r_b^2-a^2}\right]^{1/2}\right],$$

$$a < r < r_b. \tag{37}$$

The rotation velocities in Eqs. (36) and (37) are illustrated schematically in Fig. 4. In contrast to Eq. (27), where the ions in the anode region satisfy $\omega_{ri}^-(r) \simeq \text{const}$, we note from Eq. (37) that $\omega_{ri}^-(r)$ generally has a strong dependence on r for the case where the cathode electrons are partially charge neutralized by the background ions.

III. ELECTROSTATIC EIGENVALUE EQUATION

A. General eigenvalue equation

We now investigate stability properties for electrostatic perturbations about the general class of cold-fluid equilibrium profiles described in Sec. II A. The stability analysis is based on the nonrelativistic cold-fluid equations of continuity and momentum transfer together with Poisson's equation for the perturbed electric field $\delta \mathbf{E}(\mathbf{x},t) = -\nabla\delta\phi(\mathbf{x},t)$. Flute perturbations with $\partial/\partial z = 0$ are assumed, and all perturbed quantities are expressed as

$$\delta\psi(r,\theta,t) = \sum_{l=-\infty}^{\infty} \delta\psi^l(r)\exp(il\theta - i\omega t),$$

where l is the azimuthal harmonic number, and ω is the complex eigenfrequency, with $\text{Im}\,\omega > 0$ corresponding to instability. For electrostatic perturbations about a cylindrically symmetric equilibrium characterized by density profiles $n_j^0(r)$ $(j=b,e,i)$, radial electric field $E_r^0(r)$ [Eq. (5)], and equilibrium rotation velocity $\omega_{rj}^-(r)$ [Eqs. (11), (13), and (14)], the linearized continuity and cold-fluid momentum transfer equations are given by[20]

$$-i(\omega - l\omega_{rj}^-)\delta n_j^l + \frac{1}{r}\frac{\partial}{\partial r}(rn_j^0\delta V_{jr}^l) + \frac{il}{r}n_j^0\delta V_{j\theta}^l = 0, \tag{38}$$

$$-i(\omega - l\omega_{rj}^-)\delta V_{jr}^l - (\epsilon_j\omega_{cj} + 2\omega_{rj}^-)\delta V_{j\theta}^l = -\frac{e_j}{m_j}\frac{\partial}{\partial r}\delta\phi^l, \tag{39}$$

$$-i(\omega - l\omega_{rj}^-)\delta V_{j\theta}^l + \left[\epsilon_j\omega_{cj} + \frac{1}{r}\frac{\partial}{\partial r}(r^2\omega_{rj}^-)\right]\delta V_{jr}^l$$
$$= -\frac{e_j}{m_j}\frac{il\delta\phi^l}{r}. \tag{40}$$

Here, $\delta n_j^l(r)$, $\delta V_{jr}^l(r)$, and $\delta V_{j\theta}^l(r)$ are the Fourier amplitudes for the perturbed density, radial flow velocity, and azimuthal flow velocity, respectively, and the notation is

otherwise identical to Sec. II A. Moreover, the perturbed potential amplitude $\delta\phi^l(r)$ is determined self-consistently in terms of $\delta n_j^l(r)$ from Poisson's equation

$$\frac{1}{r}\frac{\partial}{\partial r}\left[r\frac{\partial}{\partial r}\delta\phi^l\right] - \frac{l^2}{r^2}\delta\phi^l = -\sum_j 4\pi e_j\delta n_j^l, \tag{41}$$

where the summation $\sum_j$ is over all plasma components $j = b,e,i$.

After some straightforward algebra that utilizes Eqs. (38)–(40) to express δn_j^l in terms of $\delta\phi^l$, Poisson's equation (41) can be expressed as[20]

$$\frac{1}{r}\frac{\partial}{\partial r}\left[r\left[1+\sum_j\chi_j\right]\frac{\partial}{\partial r}\delta\phi^l\right] - \frac{l^2}{r^2}\left[1+\sum_j\chi_j\right]\delta\phi^l$$
$$= \frac{-l\delta\phi^l}{r}\sum_j\frac{1}{\omega-l\omega_{rj}^-}\frac{\partial}{\partial r}\left[\frac{\omega_{pj}^2(\epsilon_j\omega_{cj}+2\omega_{rj}^-)}{v_j^2}\right], \tag{42}$$

where $\omega_{pj}^2(r) = 4\pi n_j^0(r)e_j^2/m_j$, and the effective susceptibility $\chi_j(r,\omega)$ for component j is defined by

$$\chi_j(r,\omega) = -\frac{\omega_{pj}^2(r)}{v_j^2(r,\omega)}, \tag{43}$$

where

$$v_j^2(r,\omega) = (\omega - l\omega_{rj}^-)^2$$
$$- (\epsilon_j\omega_{cj}+2\omega_{rj}^-)\left[\epsilon_j\omega_{cj} + \frac{1}{r}\frac{\partial}{\partial r}(r^2\omega_{rj}^-)\right]. \tag{44}$$

For general equilibrium profiles $n_j^0(r)$, the rotation velocities $\omega_{rj}^-(r)$ occurring in Eqs. (42) and (44) are determined self-consistently from Eqs. (13) and (14) for plasma components $j = b,e,i$. The eigenvalue equation (42) for $\delta\phi^l$ must of course be solved subject to the boundary conditions

$$\delta\phi^l(r=a) = 0 = \delta\phi^l(r=b) \tag{45}$$

at the cathode $(r=a)$ and anode $(r=b)$. Making use of the equilibrium force balance equation (11) and Poisson's equation (4), the expression for $v_j^2(r,\omega)$ in Eq. (44) can be further simplified. In particular, it can be shown that

$$(\epsilon_j\omega_{cj}+2\omega_{rj}^-)\left[\epsilon_j\omega_{cj} + \frac{1}{r}\frac{\partial}{\partial r}(r^2\omega_{rj}^-)\right]$$
$$= \omega_{cj}^2 + 2\epsilon_j\omega_{cj}\omega_E(r) - \frac{4\pi e_j}{m_j}\sum_k e_k n_k^0(r), \tag{46}$$

where $\omega_E(r)$ is defined in Eq. (10), and the summation $\sum_k$ extends over all plasma components $k = b,e,i$. Substituting Eq. (46) into Eq. (44) then gives

$$v_j^2(r,\omega) = (\omega - l\omega_{rj}^-)^2$$
$$- \left[\omega_{cj}^2 + 2\epsilon_j\omega_{cj}\omega_E(r) - \frac{4\pi e_j}{m_j}\sum_k e_k n_k^0(r)\right]. \tag{47}$$

To summarize, Eq. (42) is the electrostatic eigenvalue

equation that determines the eigenfunction $\delta\phi^l(r)$ and the complex eigenfrequency ω for general equilibrium density profiles $n_j^0(r)$, $j=b,e,i$. The quantities $\chi_j(r,\omega)$ and $v_j^2(r,\omega)$ are defined in Eqs. (43) and (44), and $\omega_E(r)$ and $\omega_{rj}^-(r)$ are determined self-consistently from Eqs. (10), (13), and (14).

B. Eigenvalue equation for rectangular density profiles

We now simplify the eigenvalue equation (42) for the perturbations about the equilibrium discussed in Sec. II B and illustrated in Fig. 2. The density profiles are assumed to be rectangular [Eqs. (15)–(17)] and there is a neutral plasma in the vicinity of the anode. The eigenvalue equation (42) can be expressed as

$$\frac{1}{r}\frac{\partial}{\partial r}\left[r\left(1+\sum_j \chi_j\right)\frac{\partial}{\partial r}\delta\phi^l\right]-\frac{l^2}{r^2}\left(1+\sum_j \chi_j\right)\delta\phi^l$$

$$=\frac{l\delta\phi^l}{r}\sum_j\frac{1}{\omega-l\omega_{rj}^-}\frac{\partial}{\partial r}[\chi_j(\epsilon_j\omega_{cj}+2\omega_{rj}^-)]\ ,\quad(48)$$

where $\chi_j(r,\omega)$ is defined in Eq. (43).

For the electrons in the cathode region $(j=b)$, referring to Sec. II B and Fig. 2, the effective susceptibility is

$$\chi_b(r,\omega)=\begin{cases}-\dfrac{\hat{\omega}_{pb}^2}{v_b^2},&a<r<r_b\\[2mm]0,&r_b<r<b\end{cases}\quad(49)$$

where v_b^2 is defined by [Eq. (47)]

$$v_b^2(r,\omega)=(\omega-l\omega_{rb}^-)^2-[\omega_{ce}^2-\hat{\omega}_{pb}^2-2\omega_{ce}\omega_E(r)]$$

$$=(\omega-l\omega_{rb}^-)^2-\left[\omega_{ce}^2-\hat{\omega}_{pb}^2-\hat{\omega}_{pb}^2\left(\frac{r^2-a^2}{r^2}\right)\right]$$

(50)

for $a<r<r_b$. Here, $\hat{\omega}_{pb}^2=4\pi\hat{n}_b e^2/m_e$, and $\omega_{rb}^-(r)$ is defined in Eq. (19).

For the plasma ions in the anode region $(j=i)$, the effective susceptibility $\chi_i(r,\omega)$ is

$$\chi_i(r,\omega)=\begin{cases}0,&a<r<r_p\\[2mm]-\dfrac{\hat{\omega}_{pi}^2}{v_i^2},&r_p<r<b\end{cases}\quad(51)$$

where $\hat{\omega}_{pi}^2=4\pi\hat{n}_i Z_i^2 e^2/m_i$, and v_i^2 is defined by [Eq. (47)]

$$v_i^2(r,\omega)=(\omega-l\omega_{ri}^-)^2-[\omega_{ci}^2+2\omega_{ci}\omega_E(r)]$$

$$=(\omega-l\omega_{ri}^-)^2-\left[\omega_{ci}^2+\frac{Z_i m_e}{m_i}\hat{\omega}_{pb}^2\left(\frac{r_b^2-a^2}{r^2}\right)\right]$$

(52)

for $r_p<r<b$. In obtaining Eq. (52) from Eq. (47), we have made use of charge neutrality $[\sum_{j=i,e}n_j^0(r)e_j=0]$ of the anode plasma [Eq. (17)]. Moreover, $\omega_{ri}^-(r)$ is defined in Eq. (21).

Finally, for the plasma electrons in the anode region $(j=e)$, the effective susceptibility $\chi_e(r,\omega)$ is

$$\chi_e(r,\omega)=\begin{cases}0,&a<r<r_p\\[2mm]-\dfrac{\hat{\omega}_{pe}^2}{v_e^2},&r_p<r<b\end{cases}\quad(53)$$

where $\hat{\omega}_{pe}^2=4\pi\hat{n}_e e^2/m_e$, and v_e^2 is defined by [Eq. (47)]

$$v_e^2(r,\omega)=(\omega-l\omega_{re}^-)^2-[\omega_{ce}^2-2\omega_{ce}\omega_E(r)]$$

$$=(\omega-l\omega_{re}^-)^2-\left[\omega_{ce}^2-\hat{\omega}_{pb}^2\left(\frac{r_b^2-a^2}{r^2}\right)\right]\quad(54)$$

for $r_p<r<b$. Here $\omega_{re}^-(r)$ is defined in Eq. (20) for the plasma electrons in the anode region.

To summarize, the eigenvalue equation (48), together with the definitions in Eqs. (19)–(21) and (49)–(54) constitute the final eigenvalue equation for electrostatic perturbations about the equilibrium density profiles specified by Eqs. (15)–(17). In this regard, within the context of the present nonrelativistic, electrostatic, cold-fluid model, the eigenvalue equation (48) is exact. That is, there is no a priori assumption that the diode aspect ratio is large, that the density is low, etc. Therefore, Eqs. (48)–(54) have a wide range of applicability.

The detailed stability properties predicted by Eq. (48) are analyzed numerically in Sec. V for a wide range of equilibrium parameters. In Sec. IV, we investigate Eq. (48) in the low-density, low-frequency regime where the solutions are analytically tractable.

IV. ION RESONANCE INSTABILITY DRIVEN BY ANODE PLASMA IONS

A. Simplified eigenvalue equation

As an example that is analytically tractable, we consider the eigenvalue equation (48) for the case of a low-density anode plasma with

$$\hat{n}_i,\hat{n}_e\ll\hat{n}_b\ ,\quad(55)$$

and strongly magnetized cathode electrons with

$$\omega_{pb}^2(r)\ll\omega_{ce}^2\ .\quad(56)$$

The equilibrium configuration, effective susceptibilities, etc., correspond to the rectangular profiles considered in Secs. II B and III B with the following additional simplifying assumptions.

(a) The cylindrical diode has large aspect ratio with

$$\frac{(b-a)^2}{a^2}\ll1\ .\quad(57)$$

(b) We examine Eq. (48) for low-frequency perturbations with

$$|\omega-l\omega_{rb}^-(r)|^2\ll\omega_{ce}^2\ .\quad(58)$$

(c) The anode plasma extends to the edge of the cathode electrons with

$$r_p=r_b\quad(59)$$

as illustrated in Fig. 5.

Consistent with Eqs. (56) and (57), the angular rotation

velocity of the cathode electrons can be approximated by [see also Eqs. (19) and (24)]

$$\omega_{rb}^-(r) = \omega_E(r)$$

$$= \frac{\hat{\omega}_{pb}^2}{2\omega_{ce}} \left[\frac{r^2 - a^2}{r^2} \right] \simeq \frac{\hat{\omega}_{pb}^2}{\omega_{ce}} \left[\frac{r - a}{r_b} \right] \tag{60}$$

for $a < r < r_b$. In Eq. (60), we have approximated $(r + a)/r^2 \simeq 2/r_b$ for the case of a large-aspect-ratio diode [Eq. (57)]. Furthermore, from Eqs. (27) and (57), we neglect the (slow) r-variation of $\omega_{ri}^-(r)$ and approximate

$$\omega_{ri}^-(r) = \hat{\omega}_{ri}^- = \frac{1}{2}[-\omega_{ci} + (\omega_{ci}^2 + 4\omega_{ci}\hat{\Omega}_E)^{1/2}] \tag{61}$$

for $r_b < r < b$, where $\hat{\Omega}_E = \omega_E(r_b)$ is given by

$$\hat{\Omega}_E = \frac{\hat{\omega}_{pb}^2}{\omega_{ce}} \left[\frac{r_b - a}{r_b} \right] . \tag{62}$$

Similarly, the rotation velocity of the electrons in the cathode region [Eqs. (20) and (25)] is approximated by $\omega_{re}^-(r) = \hat{\Omega}_E$ for $r_b < r < b$.

We now examine the susceptibility factors occurring on the left-hand side of Eq. (48). Referring to Eqs. (49) and (50), and making use of Eqs. (56), (58), and (60), we find $v_b^2 \simeq -\omega_{ce}^2$. Therefore, χ_b can be approximated by

$$\chi_b(r,\omega) = \begin{cases} \dfrac{\hat{\omega}_{pb}^2}{\omega_{ce}^2}, & a < r < r_b \\[2ex] 0, & r_b < r < b . \end{cases} \tag{63}$$

Note that $|\chi_b| \ll 1$ since $\hat{\omega}_{pb}^2 \ll \omega_{ce}^2$ is assumed. Similarly, from Eqs. (53) and (54), it can be shown for the electrons in the anode region that $\chi_e(r,\omega) \simeq \hat{\omega}_{pe}^2/\omega_{ce}^2$ over the range $r_b < r < b$. Moreover, $|\chi_e| \ll 1$ by virtue of Eqs. (55) and (56). Finally, from Eqs. (51), (52), (61), and (62), the ion susceptibility $\chi_i(r,\omega)$ can be expressed as

$$\chi_i(r,\omega) = \begin{cases} 0, & a < r < r_b \\[2ex] -\dfrac{\hat{\omega}_{pi}^2}{(\omega - l\hat{\omega}_{ri}^-)^2 - (\omega_{ci}^2 + 2\omega_{ci}\hat{\Omega}_E)}, & r_b < r < b \end{cases} \tag{64}$$

where $\hat{\omega}_{ri}^-$ and $\hat{\Omega}_E$ are defined in Eqs. (61) and (62).

With regard to the right-hand side of the eigenvalue equation (48), we retain the perturbed surface-charge contribution from the cathode electrons, which is proportional to $\partial\omega_{pb}^2(r)/\partial r = -\hat{\omega}_{pb}^2\delta(r - r_b)$. However, we neglect the perturbed surface-charge contributions from the anode plasma electrons and ions $(j = e,i)$ by virtue of the low-density assumption in Eq. (55). Approximating

$$\frac{\omega_{pb}^2(r)}{v_b^2(r,\omega)}(-\omega_{ce} + 2\omega_{rb}^-) = \frac{\omega_{pb}^2(r)}{\omega_{ce}} \tag{65}$$

on the right-hand side of Eq. (48), and $|\chi_b| \ll 1$ and $|\chi_e| \ll 1$ on the left-hand side of Eq. (48), the eigenvalue equation can be expressed as

$$\frac{1}{r}\frac{\partial}{\partial r}\left\{ r[1 + \chi_i(r,\omega)]\frac{\partial}{\partial r}\delta\phi^l \right\} - \frac{l^2}{r^2}[1 + \chi_i(r,\omega)]\delta\phi^l$$

$$= \frac{l\delta\phi^l}{r}\frac{(\hat{\omega}_{pb}^2/\omega_{ce})}{\omega - l\omega_E(r)}\delta(r - r_b) , \tag{66}$$

where $\chi_i(r,\omega)$ is defined in Eq. (64).

To summarize, Eq. (66) is an excellent approximation to the exact eigenvalue equation (48) in circumstances where the anode plasma density is low [Eq. (55)], the cathode electrons are strongly magnetized [Eq. (56)], the diode aspect ratio is large [Eq. (57)], and the perturbation frequency is low [Eq. (58)]. It is clear from Eq. (66) that the surface-charge perturbation on the cathode electrons can couple to the dielectric response of the plasma ions in the anode region.

B. Dispersion relation and analytic results

In this section, we solve the approximate eigenvalue equation (66) subject to the boundary conditions $\delta\phi^l(r = a) = 0 = \delta\phi^l(r = b)$. Referring to Fig. 5, in region I $(a < r < r_b)$, Eq. (66) reduces to $(1/r)(\partial/\partial r)(r\partial\delta\phi^l/\partial r) - (l^2/r^2)\delta\phi^l = 0$, which has the solution

$$\delta\phi_I^l(r) = A \left[\left[\frac{r}{a} \right]^l - \left[\frac{a}{r} \right]^l \right]$$

$$\times \left[\left[\frac{r_b}{a} \right]^l - \left[\frac{a}{r_b} \right]^l \right]^{-1} , \quad a < r < r_b . \tag{67}$$

Moreover, in region II $(r_b < r < b)$, Eq. (66) again reduces to $(1/r)(\partial/\partial r)(r\partial\delta\phi^l/\partial r) - (l^2/r^2)\delta\phi^l = 0$. The solution for $\delta\phi^l(r)$ in region II that is continuous with Eq. (67) at
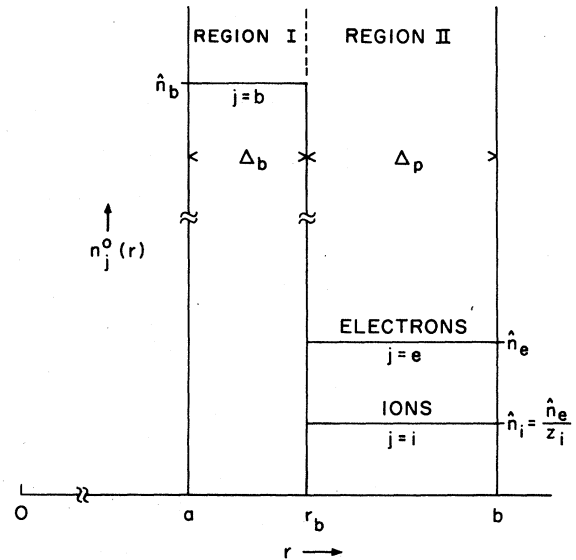

FIG. 5. Model density profiles used for electrostatic stability analysis in Sec. IV. Anode plasma density is low with $\hat{n}_i, \hat{n}_e \ll \hat{n}_b$ [Eq. (55)], and the anode plasma extends to the edge of the cathode electrons with $r_p = r_b$ [Eq. (59)].

$r = r_b$ and vanishes at $r = b$ is given by

$$\delta\phi_{\mathrm{II}}^l(r) = A \left[\left[\frac{r}{b}\right]^l - \left[\frac{b}{r}\right]^l \right]$$

$$\times \left[\left[\frac{r_b}{b}\right]^l - \left[\frac{b}{r_b}\right]^l \right]^{-1} , \quad r_b < r < b . \quad (68)$$

The remaining boundary condition is obtained by integrating Eq. (66) across the surface at $r = r_b$ (Fig. 5). Multiplying Eq. (66) by r and integrating from $r_b(1-\delta)$ to $r_b(1+\delta)$ with $\delta \rightarrow 0_+$ gives

$$r_b \left[1 - \frac{\hat{\omega}_{pi}^2}{(\omega - l\hat{\omega}_{ri}^-)^2 - (\omega_{ci}^2 + 2\omega_{ci}\hat{\Omega}_E)} \right] \left[\frac{\partial}{\partial r}\delta\phi_{\mathrm{II}}^l \right]_{r=r_b}$$

$$-r_b \left[\frac{\partial}{\partial r}\delta\phi_{\mathrm{I}}^l \right]_{r=r_b} = \frac{l\delta\phi_{\mathrm{I}}^l(r_b)}{\omega - l\omega_E(r_b)} \frac{\hat{\omega}_{pb}^2}{\omega_{ce}} . \quad (69)$$

Equation (69) relates the discontinuity in $(\partial\delta\phi^l/\partial r)$ at $r = r_b$ to the perturbed surface-charge density.

We define

$$r_b - a = \Delta_b ,$$
$$b - r_b = \Delta_p , \quad (70)$$

where Δ_b is the width of the cathode electron region and Δ_p is the width of the anode plasma region (Fig. 5). Moreover, from Eqs. (60) and (70),

$$\omega_E(r_b) = \hat{\Omega}_E = \frac{\hat{\omega}_{pb}^2}{\omega_{ce}} \frac{\Delta_b}{r_b} . \quad (71)$$

Substituting Eqs. (67) and (68) into Eq. (69) then gives

$$-l \left[1 - \frac{\hat{\omega}_{pi}^2}{(\omega - l\hat{\omega}_{ri}^-)^2 - (\omega_{ci}^2 + 2\omega_{ci}\hat{\Omega}_E)} \right] \frac{1 + (r_b/b)^{2l}}{1 - (r_b/b)^{2l}}$$

$$-l\frac{1 + (a/r_b)^{2l}}{1 - (a/r_b)^{2l}} = \frac{r_b}{\Delta_b} \frac{l\hat{\Omega}_E}{\omega - l\hat{\Omega}_E} . \quad (72)$$

Equation (72) plays the role of a dispersion relation that determines the complex eigenfrequency ω in terms of other system parameters.

For a large-aspect-ratio diode, we Taylor-series expand $[1 + (r_b/b)^{2l}]/[1 - (r_b/b)^{2l}] \simeq b/l\Delta_p$ and $[1 + (a/r_b)^{2l}]/[1 - (a/r_b)^{2l}] \simeq a/l\Delta_b$, where

$$\frac{l\Delta_p}{b}, \frac{l\Delta_b}{a} \ll 1 \quad (73)$$

is assumed. Equation (72) then reduces to

$$1 + \frac{\Delta_p}{\Delta_b} \frac{r_b}{b} - \frac{\hat{\omega}_{pi}^2}{(\omega - l\hat{\omega}_{ri}^-)^2 - (\omega_{ci}^2 + 2\omega_{ci}\hat{\Omega}_E)}$$

$$= -\frac{r_b}{b} \frac{\Delta_p}{\Delta_b} \frac{l\hat{\Omega}_E}{\omega - l\hat{\Omega}_E} . \quad (74)$$

Taking $r_b/b \simeq 1$ in Eq. (74) for a large-aspect-ratio diode gives the approximate dispersion relation

$$\left[1 + \frac{\Delta_p}{\Delta_b} \right] - \frac{\hat{\omega}_{pi}^2}{(\omega - l\hat{\omega}_{ri}^-)^2 - (\omega_{ci}^2 + 2\omega_{ci}\hat{\Omega}_E)}$$

$$= -\frac{\Delta_p}{\Delta_b} \frac{l\hat{\Omega}_E}{\omega - l\hat{\Omega}_E} . \quad (75)$$

For the special case of no ions ($\hat{\omega}_{pi}^2 = 0$), Eq. (75) gives the familiar result

$$\omega - l\hat{\Omega}_E = -\frac{\Delta_p}{\Delta_b + \Delta_p} l\hat{\Omega}_E \quad (76)$$

corresponding to stable oscillations on the surface of the electron layer. For $\hat{\omega}_{pi}^2 \neq 0$, however, Eq. (75) can give instability associated with the coupling of these surface oscillations to the plasma ions in the anode region.

Making use of the definitions $\hat{\omega}_{pi}^2 = 4\pi\hat{n}_i Z_i^2 e^2/m_i$ and $\hat{\Omega}_E = (\hat{\omega}_{pb}^2/\omega_{ce})(\Delta_b/r_b)$ [Eq. (62)], two of the dimensionless frequencies occurring in the dispersion relation (75) can be expressed for a large-aspect-ratio diode as

$$\frac{\omega_{ci}}{\hat{\Omega}_E} = \frac{Z_i m_e}{m_i} \frac{\omega_{ce}^2}{\hat{\omega}_{pb}^2} \frac{r_b}{\Delta_b} , \quad (77)$$

$$\frac{\hat{\omega}_{pi}^2}{\hat{\Omega}_E^2} = \frac{Z_i m_e}{m_i} \frac{Z_i \hat{n}_i}{\hat{n}_b} \frac{\omega_{ce}^2}{\hat{\omega}_{pb}^2} \frac{r_b^2}{\Delta_b^2}$$

$$= \frac{Z_i \hat{n}_i}{\hat{n}_b} \frac{r_b}{\Delta_b} \frac{\omega_{ci}}{\hat{\Omega}_E} . \quad (78)$$

Moreover, from Eq. (61), $\hat{\omega}_{ri}^-/\hat{\Omega}_E$ is given by

$$\frac{\hat{\omega}_{ri}^-}{\hat{\Omega}_E} = \frac{1}{2} \left[-\frac{\omega_{ci}}{\hat{\Omega}_E} + \left[\frac{\omega_{ci}^2}{\hat{\Omega}_E^2} + 4\frac{\omega_{ci}}{\hat{\Omega}_E} \right]^{1/2} \right] . \quad (79)$$

The dispersion relation (75) is a cubic equation for the complex eigenfrequency ω, valid for a large-aspect-ratio diode within the context of the assumptions enumerated at the beginning of Sec. IV A. Making use of Eq. (75), the marginal stability curves (Im$\omega = 0$) in the parameter space $(\omega_{ci}/\hat{\Omega}_E, \hat{\omega}_{pi}^2/\hat{\Omega}_E^2)$ are plotted in Fig. 6 for several values of azimuthal harmonic number l and for $\Delta_b/\Delta_p = 3$ [Fig. 6(a)], $\Delta_b/\Delta_p = 1$ [Fig. 6(b)], and $\Delta_b/\Delta_p = \frac{1}{3}$ [Fig. 6(c)]. For specified l, the regions above the curves in Fig. 6 correspond to instability with Im$\omega > 0$, whereas the regions below the curves correspond to stable oscillations with Im$\omega = 0$. Moreover, for the choice of system parameters $\hat{\omega}_{ci}/\hat{\Omega}_E = 0.1$ and $\Delta_b/\Delta_p = 1$, shown in Fig. 7 are plots of normalized growth rate (Imω)/$\hat{\Omega}_E$ [Fig. 7(a)] and real frequency (Reω)/$\hat{\Omega}_E$ [Fig. 7(b)] versus $\hat{\omega}_{pi}^2/\hat{\Omega}_E^2$ obtained from Eq. (75). Several features of the stability behavior are noteworthy from Figs. 6 and 7.

(a) First, for weakly magnetized ions with $\omega_{ci}/\hat{\Omega}_E \ll 1$, it follows from Fig. 6 that instability can exist over a relatively wide range of ion density as measured by $\hat{\omega}_{pi}^2/\hat{\Omega}_E^2$.

(b) Typically, for specified $\omega_{ci}/\hat{\Omega}_E$, Δ_b/Δ_p, and harmonic number l, there is a threshold value of ion density above which instability occurs. For example, for $\omega_{ci}/\hat{\Omega}_E = 0.01$ and a relatively thick cathode electron layer with $\Delta_b/\Delta_p = 3$, it follows from Fig. 6(a) that instability occurs when $\hat{\omega}_{pi}^2/\hat{\Omega}_E^2 > 0.06$ for the $l = 1$ mode, and when $\hat{\omega}_{pi}^2/\hat{\Omega}_E^2 > 0.5$ for the $l = 2$ mode. On the other
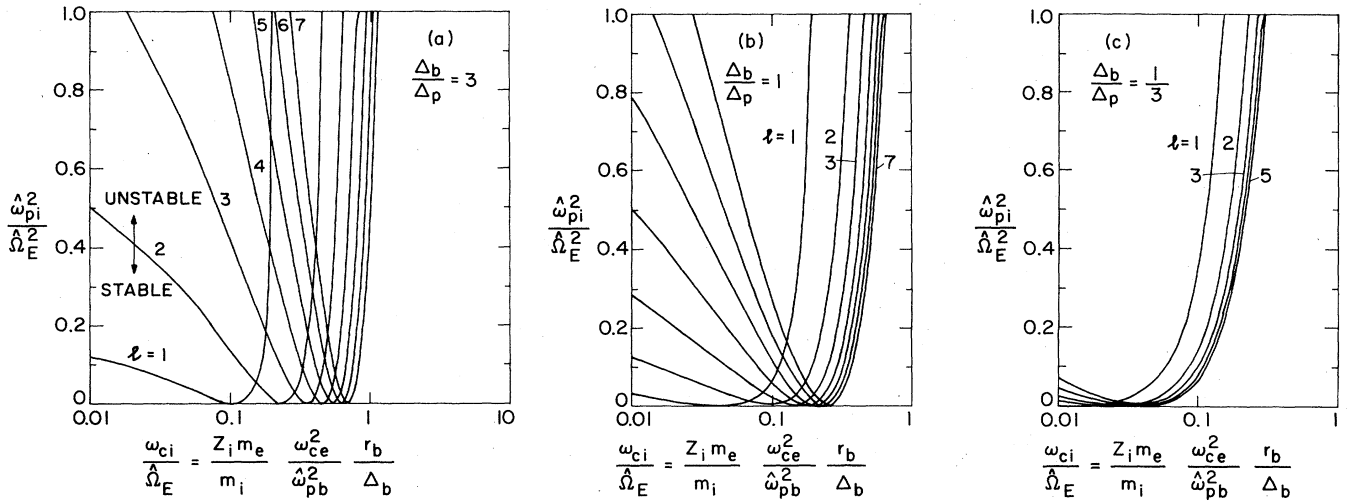
FIG. 6. Plots of marginal stability curves in the parameter space $(\omega_{ci}/\hat{\Omega}_E, \hat{\omega}_{pi}^2/\hat{\Omega}_E^2)$ obtained from Eq. (75) for several values of harmonic number l and (a) $\Delta_b/\Delta_p = 3$, (b) $\Delta_b/\Delta_p = 1$, and (c) $\Delta_b/\Delta_p = \frac{1}{3}$. Regions above the curves are unstable (Im$\omega > 0$), and regions below the curves correspond to stable oscillations (Im$\omega = 0$).

hand, for $\omega_{ci}/\hat{\Omega}_E = 0.01$ and $\Delta_b/\Delta_p = \frac{1}{3}$, which corresponds to a relatively thick anode plasma region and thin cathode electron layer (see Fig. 5), we find from Fig. 6(c) that the threshold for instability occurs at much lower values of $\hat{\omega}_{pi}^2/\hat{\Omega}_E^2$ than the $\Delta_b/\Delta_p = 3$ case analyzed in Fig. 6(a).

(c) From Eq. (75), it can be shown that the minima in the marginal stability curves plotted in Fig. 6 occur for $\hat{\omega}_{pi}^2/\hat{\Omega}_E^2 = 0$ and values of $\omega_{ci}/\hat{\Omega}_E$ determined from

$$\frac{2\Delta_b}{\Delta_b + \Delta_p} = \left[(\eta^2 + 4\eta)^{1/2} - \eta + \frac{2}{l}(\eta^2 + 2\eta)^{1/2} \right]_{\eta = (\omega_{ci}/\hat{\Omega}_E)_M}$$

(80)

for $l = 1, 2, \ldots$. When $\omega_{ci}/\hat{\Omega}_E$ is less than the value of $(\omega_{ci}/\hat{\Omega}_E)_M$ for $l = 1$, it is evident from Fig. 6 that the $l = 1, 2, \ldots$ modes switch on sequentially as $\hat{\omega}_{pi}^2/\hat{\Omega}_E^2$ is increased. On the other hand, when $\omega_{ci}/\hat{\Omega}_E$ exceeds the value of $(\omega_{ci}/\hat{\Omega}_E)_M$ for $l = 1$, it follows from Fig. 6 that selected higher mode numbers have a lower threshold value of $\hat{\omega}_{pi}^2/\hat{\Omega}_E^2$ for instability than the $l = 1$ mode (see also Fig. 7).

(d) As a general remark, for specified $\hat{\omega}_{pi}^2/\hat{\Omega}_E^2$ and mode number l, it is evident from Fig. 6 that the range of $\omega_{ci}/\hat{\Omega}_E$ corresponding to instability shifts upward as the thickness of the cathode electron layer is increased relative to the thickness of the anode plasma region. For example, for $\hat{\omega}_{pi}^2/\hat{\Omega}_E^2 = 1$ and $l = 7$, it follows from Figs. 6(a) and
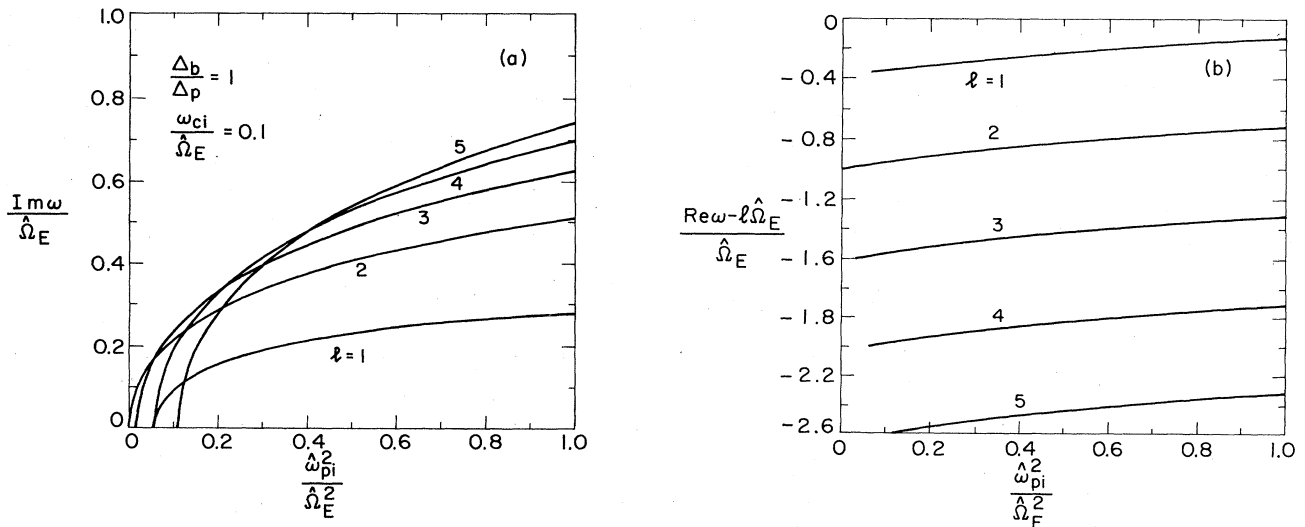

FIG. 7. Plots of (a) normalized growth rate (Im$\omega)/\hat{\Omega}_E$ and (b) normalized real oscillation frequency (Re$\omega - l\hat{\Omega}_E)/\hat{\Omega}_E$ vs $\hat{\omega}_{pi}^2/\hat{\Omega}_E^2$ obtained from Eq. (75) for $\Delta_b/\Delta_p = 1$, $\omega_{ci}/\hat{\Omega}_E = 0.1$, and several values of harmonic number l.

6(c) that instability exists for $0.026 < \omega_{ci}/\widehat{\Omega}_E < 0.65$ when $\Delta_b/\Delta_p = 1$, and for $0.26 < \omega_{ci}/\widehat{\Omega}_E < 1$ when $\Delta_b/\Delta_p = 3$.

(e) In Fig. 7, we plot the normalized growth rate $(\text{Im}\omega)/\widehat{\Omega}_E$ [Fig. 7(a)] and real frequency $(\text{Re}\omega)/\widehat{\Omega}_E$ [Fig. 7(b)] versus $\widehat{\omega}_{pi}^2/\widehat{\Omega}_E^2$ obtained from Eq. (75) for $\Delta_b/\Delta_p = 1$, $\omega_{ci}/\widehat{\Omega}_E = 0.1$, and $l = 1, 2, \ldots, 5$. Referring to Figs. 6(b) and 7(a), we find that as $\widehat{\omega}_{pi}^2/\widehat{\Omega}_E^2$ is increased, the unstable modes switch on sequentially in the order $l = 2$, $l = 3$, $l = 1$ and $l = 4$, and $l = 5$. Moreover, the growth rates for the ion resonance instability inferred from Fig. 7(a) can be substantial. For example, for $l = 3$ and $\widehat{\omega}_{pi}^2/\Omega_E^2 = 0.5$, it follows from Fig. 7(a) that $\text{Im}\omega \simeq 0.5\widehat{\Omega}_E = 0.707\widehat{\omega}_{pi}$. Moreover, for $l = 3$ and $\widehat{\omega}_{pi}^2/\Omega_E^2 = 0.5$, the real oscillation frequency is $\text{Re}\omega \simeq -1.42\widehat{\Omega}_E = -2\widehat{\omega}_{pi}$ [Fig. 7(b)].

To summarize, in Sec. IV we have investigated analytically properties of the ion resonance instability[12] in circumstances where the anode plasma density is low [Eq. (55)], the cathode electrons are strongly magnetized [Eq. (56)], the diode aspect ratio is large [Eq. (57)], the perturbation frequency is low [Eq. (58)], and the anode plasma is in contact with the cathode electrons [Eq. (59) and Fig. 5]. Although these assumptions are somewhat restrictive, the analysis clearly establishes the existence and qualitative features of the ion resonance instability and the fact that the plasma ions in the anode region can strongly couple to the cathode electrons.

V. DIOCOTRON INSTABILITY DRIVEN BY ANODE PLASMA ELECTRONS

As a second example that is analytically tractable, we consider the eigenvalue equation (48) in circumstances where the anode plasma is not in contact with the cathode electrons, i.e.,

$$r_p > r_b \tag{81}$$

as illustrated in Fig. 2. In this case, the cathode electrons and the anode plasma electrons can combine to give the diocotron instability driven by electron velocity shear over the interval $a < r < b$. To simplify the analysis and to distinguish this instability from the ion resonance instability discussed in Sec. IV, we make the following additional assumptions.

(a) The maximum rotation frequency of the cathode electrons, $\omega_{rb}^-(r_b) = \widehat{\Omega}_E$ is much higher than the ion cyclotron frequency, i.e.,

$$\widehat{\Omega}_E \gg \omega_{ci} . \tag{82}$$

(b) Consistent with Eq. (82), we consider high-frequency perturbations with

$$\omega \approx l\omega_{rb}^-(r_b) , \tag{83}$$

and treat the anode ions as a tenuous, unmagnetized plasma component satisfying

$$|\omega| \gg \omega_{ci}, \widehat{\omega}_{pi}, |l\omega_{ri}^-(r_p)| . \tag{84}$$

(c) No a priori assumption is made regarding the relative size of the plasma electron density and the cathode electron density $(\widehat{n}_e/\widehat{n}_b)$. However, for present purposes,

it is assumed that

$$\widehat{\omega}_{pb}^2, \widehat{\omega}_{pe}^2 \ll \omega_{ce}^2 , \tag{85}$$

which corresponds to low-density, strongly magnetized electrons.

Making use of Eqs. (82)—(85), it is straightforward to simplify the eigenvalue equation (48) and the related definitions in Eqs. (49)—(54). In particular, the ions are treated as infinitely massive $(m_i \to \infty)$ and the susceptibilities $X_j(r,\omega)$ $(j = b, e, i)$ are approximated by zero on the left-hand side of Eq. (48). Moreover, only the cathode electrons and the anode electrons contribute on the right-hand side of Eq. (48). Making use of Eqs. (82)—(85), the eigenvalue equation (48) can then be approximated by

$$\frac{1}{r}\frac{\partial}{\partial r}r\frac{\partial}{\partial r}\delta\phi^l - \frac{l^2}{r^2}\delta\phi^l$$
$$= \frac{l\delta\phi^l}{r}\frac{\widehat{\omega}_{pb}^2}{\omega_{ce}}\left[\frac{\delta(r-r_b)}{\omega - l\widehat{\Omega}_E} - \frac{\widehat{n}_e}{\widehat{n}_b}\frac{\delta(r-r_p)}{\omega - l\widehat{\Omega}_E r_b^2/r_p^2}\right] . \tag{86}$$

Here, $\widehat{\omega}_{pb}^2 = 4\pi\widehat{n}_b e^2/m_e$, and $\widehat{\Omega}_E = \omega_{rb}^-(r_b) = \omega_E(r_b)$ is defined by [Eqs. (22) and (24)]

$$\widehat{\Omega}_E = \omega_D\left[\frac{r_b^2 - a^2}{r_b^2}\right] , \tag{87}$$

where

$$\omega_D = \frac{\widehat{\omega}_{pb}^2}{2\omega_{ce}} \tag{88}$$

is the effective diocotron frequency in the absence of an internal conductor $(a = 0)$. It is clear from Eq. (86) that the two source terms on the right-hand side correspond to surface-charge perturbations at the surface of the cathode electron layer $(r = r_b)$ and the anode electrons $(r = r_p)$. Also note in Eq. (86) that no a priori assumption has been made that the diode aspect ratio is large. That is, Eq. (86) is valid for arbitrary $b/a > 1$.

Referring to Fig. 2, the eigenvalue equation (86) reduces to the vacuum eigenvalue equation $r^{-1}(\partial/\partial r)(r\partial\delta\phi^l/\partial r) - (l^2/r^2)\delta\phi^l = 0$ within the cathode electron layer $(a \leq r < r_b)$, in the vacuum region $(r_b < r < r_p)$, and within the anode plasma $(r_p < r \leq b)$. Therefore, the solution to Eq. (86) that satisfies $\delta\phi^l(r = a) = 0 = \delta\phi^l(r = b)$ is given trivially by

$$\delta\phi^l(r) = \begin{cases} A\left[\left[\dfrac{r}{a}\right]^l - \left[\dfrac{a}{r}\right]^l\right], & a \leq r < r_b \\[2ex] Br^l + C/r^l, & r_b < r < r_p \\[2ex] D\left[\left[\dfrac{r}{b}\right]^l - \left[\dfrac{b}{r}\right]^l\right], & r_p < r \leq b . \end{cases} \tag{89}$$

Two of the boundary conditions required in Eq. (89) are continuity of $\delta\phi^l(r)$ at $r = r_b$ and at $r = r_p$, i.e.,

$$\lim_{\epsilon \to 0_+}\delta\phi^l(r_b - \epsilon) = \lim_{\epsilon \to 0_+}\delta\phi^l(r_b + \epsilon) ,$$

$$\lim_{\epsilon \to 0_+}\delta\phi^l(r_p - \epsilon) = \lim_{\epsilon \to 0_+}\delta\phi^l(r_p - \epsilon) . \tag{90}$$

The two remaining boundary conditions are obtained by multiplying Eq. (86) by r and integrating across the discontinuities at $r=r_b$ and at $r=r_p$. This readily gives

$$\lim_{\epsilon \to 0_+} \left[\left[r\frac{\partial}{\partial r}\delta\phi^l \right]_{r_b+\epsilon} - \left[r\frac{\partial}{\partial r}\delta\phi^l \right]_{r_b-\epsilon} \right]$$

$$= 2l\delta\phi^l(r_b)\frac{\omega_D}{\omega-l\widehat{\Omega}_E}, \quad (91)$$

and

$$\lim_{\epsilon \to 0_+} \left[\left[r\frac{\partial}{\partial r}\delta\phi^l \right]_{r_p+\epsilon} - \left[r\frac{\partial}{\partial r}\delta\phi^l \right]_{r_p-\epsilon} \right]$$

$$= -2l\delta\phi^l(r_p)\frac{\widehat{n}_e}{\widehat{n}_b}\frac{\omega_D}{\omega-l\widehat{\Omega}_E r_b^2/r_p^2}. \quad (92)$$

Substituting Eq. (89) into Eqs. (90)—(92), after some straightforward algebra we obtain the dispersion relation

$$\left[1-\left[\frac{b}{r_p}\right]^{2l} \right]\left[1+\frac{1-(a/r_b)^{2l}}{\omega/\omega_D-l(r_b^2-a^2)/r_b^2} \right]$$

$$= \left[1+\frac{(\widehat{n}_e/\widehat{n}_b)[1-(b/r_p)^{2l}]}{\omega/\omega_D-l(r_b^2-a^2)/r_p^2} \right]\left[1-\left[\frac{a}{r_p}\right]^{2l}+\left[1-\frac{r_b^{2l}}{r_p^{2l}} \right]\frac{[1-(a/r_b)^{2l}]}{\omega/\omega_D-l(r_b^2-a^2)/r_b^2} \right]. \quad (93)$$

Equation (93) can be used to determine the complex oscillation frequency ω over a wide range of system parameters $\widehat{n}_e/\widehat{n}_b$, r_b/a, r_p/a, and b/a. For the special case where the anode electrons are in contact with the cathode electrons $(r_p=r_b)$, Eq. (93) supports only stable oscillations with Im$\omega=0$. This is expected since for $r_p=r_b$ the electron density profile is monotonic over the entire interval $a<r<b$ (Fig. 2).[23]

For $r_p>r_b$, the linear dispersion relation in Eq. (93) has been solved numerically for the complex eigenfrequency ω. Typical numerical results are summarized in Fig. 8 where (a) the normalized growth rate (Imω)/ω_D and (b) the real oscillation frequency (Reω)/ω_D obtained from Eq. (93) are plotted versus r_p/a for the choice of parameters $b/a=2$, $r_b/a=1.5$, density ratio $\widehat{n}_e/\widehat{n}_b=0.1$, and several values of the azimuthal mode number l. Several points are noteworthy from Fig. 8. First, the maximum growth rate can be a substantial fraction of the diocotron frequency ω_D, thereby indicating a strong instability. Second, for each value of l, the range of r_p/a corresponding to instability (Im$\omega>0$) is relatively narrow. Evidently, from Fig. 8(a), high mode numbers l are excited when the anode plasma boundary (r_p/a) approaches the boun-

dary of the cathode electrons $(r_b/a=1.5)$. In the limit, however, instability ceases (Im$\omega=0$) when $r_p=r_b$. Finally, from Fig. 8(b), for specified value of harmonic number l, the real frequency of the unstable mode is almost independent of r_p/a.

Shown in Fig. 9 are plots of (a) the marginal stability boundaries in the parameter space $(r_p/a,l)$, and (b) the maximum growth rate and the corresponding real oscillation frequency obtained from Eq. (93) for $\widehat{n}_e/\widehat{n}_b=0.2$ and parameters otherwise identical to Fig. 8. The cross-hatched region in Fig. 9(a) corresponds to instability (Im$\omega>0$). The dashed curve in Fig. 9(a) represents the conditions for maximum growth rate. For the choice of parameters in Fig. 9, only mode numbers satisfying $l\geq 4$ exhibit instability. As shown in Fig. 9(b), the real oscillation frequency is linearly proportional to l, although the maximum growth rate saturates quickly with increasing l.

In order to illustrate the dependence of stability behavior on the density ratio $\widehat{n}_e/\widehat{n}_b$, in Fig. 10 are plotted (a) the marginal stability boundaries in the parameter space $(r_p/a,\widehat{n}_e/\widehat{n}_b)$, and (b) the maximum growth rate and the corresponding real oscillation frequency obtained from Eq. (93) for $l=5$ and parameters otherwise identical
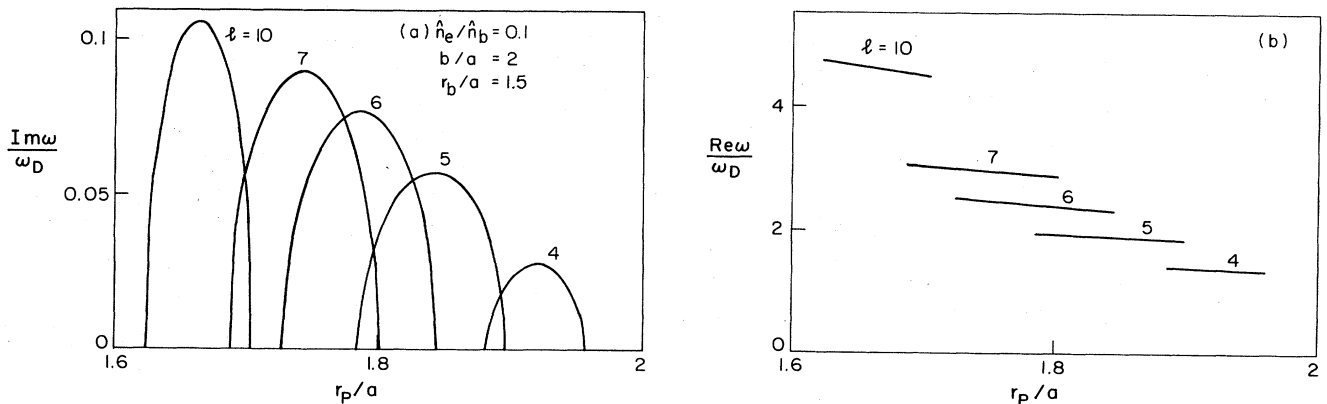

FIG. 8. Plots of (a) the normalized growth rate (Imω)/ω_D, and (b) real oscillation frequency (Reω)/ω_D vs r_p/a obtained from Eq. (93) for $b/a=2$, $r_b/a=1.5$, $\widehat{n}_e/\widehat{n}_b=0.1$ and several values of harmonic number l.
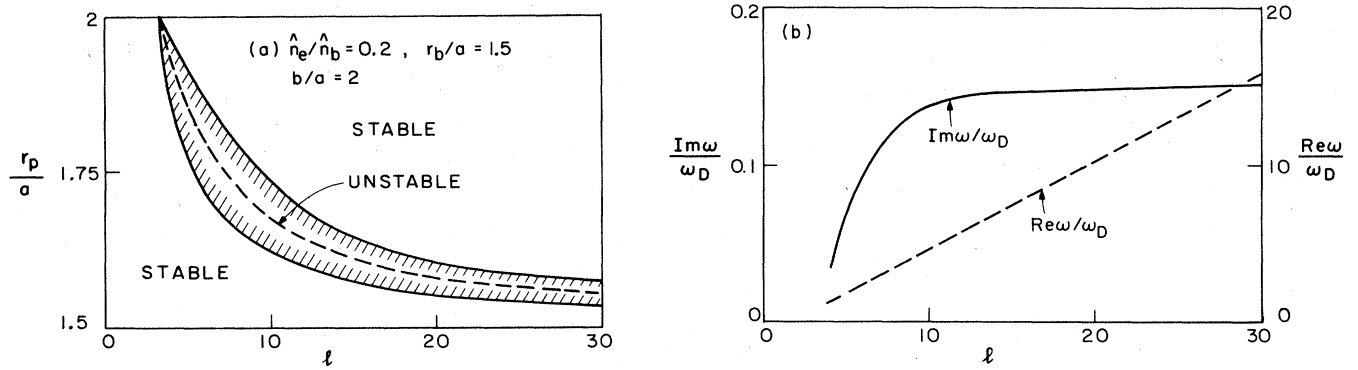
FIG. 9. Plots of (a) the marginal stability boundaries in the parameter space $(r_p/a,l)$ and (b) the maximum growth rate and corresponding real oscillation frequency obtained from Eq. (93) for $\hat{n}_e/\hat{n}_b=0.2$ and parameters otherwise identical to Fig. 8. Dashed curve in (a) corresponds to maximum growth rate.
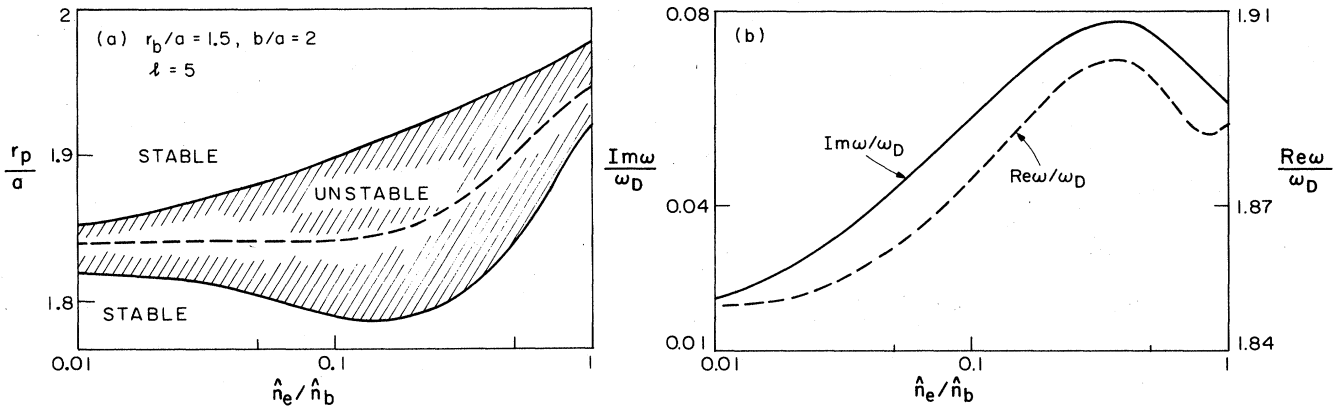

FIG. 10. Plots of (a) the marginal stability boundaries in the parameter space $(r_p/a,\hat{n}_e/\hat{n}_b)$, and (b) the maximum growth rate and corresponding real oscillation frequency obtained from Eq. (93) for $l=5$ and parameters otherwise identical to Fig. 8. Dashed curve in (a) corresponds to maximum growth rate.
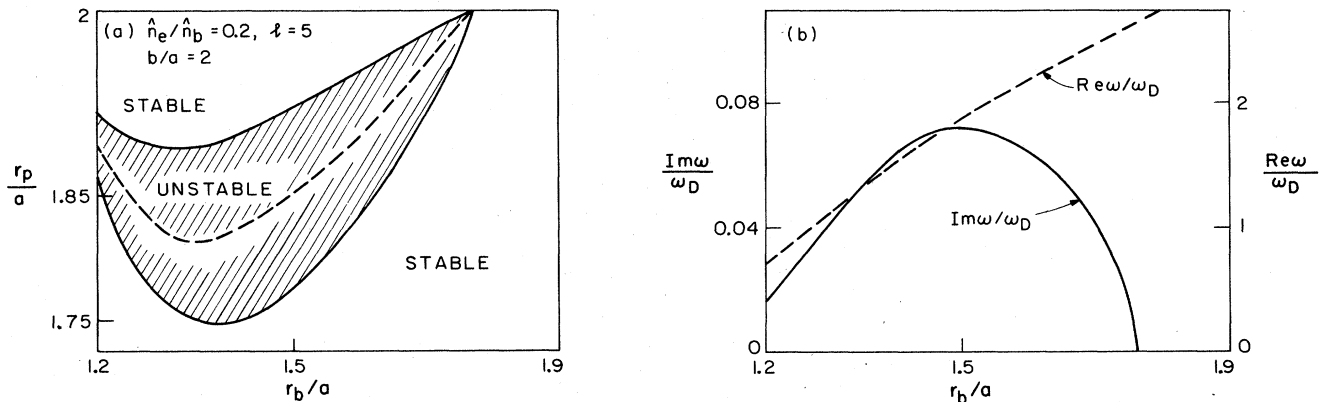

FIG. 11. Plots of (a) the marginal stability boundaries in the parameter space $(r_p/a,r_b/a)$, and (b) the maximum growth rate and corresponding real oscillation frequency obtained from Eq. (93) for $\hat{n}_e/\hat{n}_b=0.2$ and parameters otherwise identical to Fig. 10. Dashed curve in (a) corresponds to maximum growth rate.

to Fig. 8. From Fig. 10(b), for this choice of system parameters, we note that the maximum growth rate occurs for density ratio $\hat{n}_e/\hat{n}_b \simeq 0.4$. That is, the instability growth rate does not continue to increase for $\hat{n}_e/\hat{n}_b \geq 0.4$.

Finally, the dependence of stability properties on the location of the boundary of the cathode electrons (r_b/a) is illustrated in Fig. 11, where (a) the marginal stability boundaries in the parameter space $(r_p/a, r_b/a)$, and (b) the maximum growth rate and corresponding real oscillation frequency are presented for $\hat{n}_e/\hat{n}_b = 0.2$ and parameters otherwise identical to Fig. 10. The dashed curve in Fig. 11(a) corresponds to maximum growth rate. Evidently,
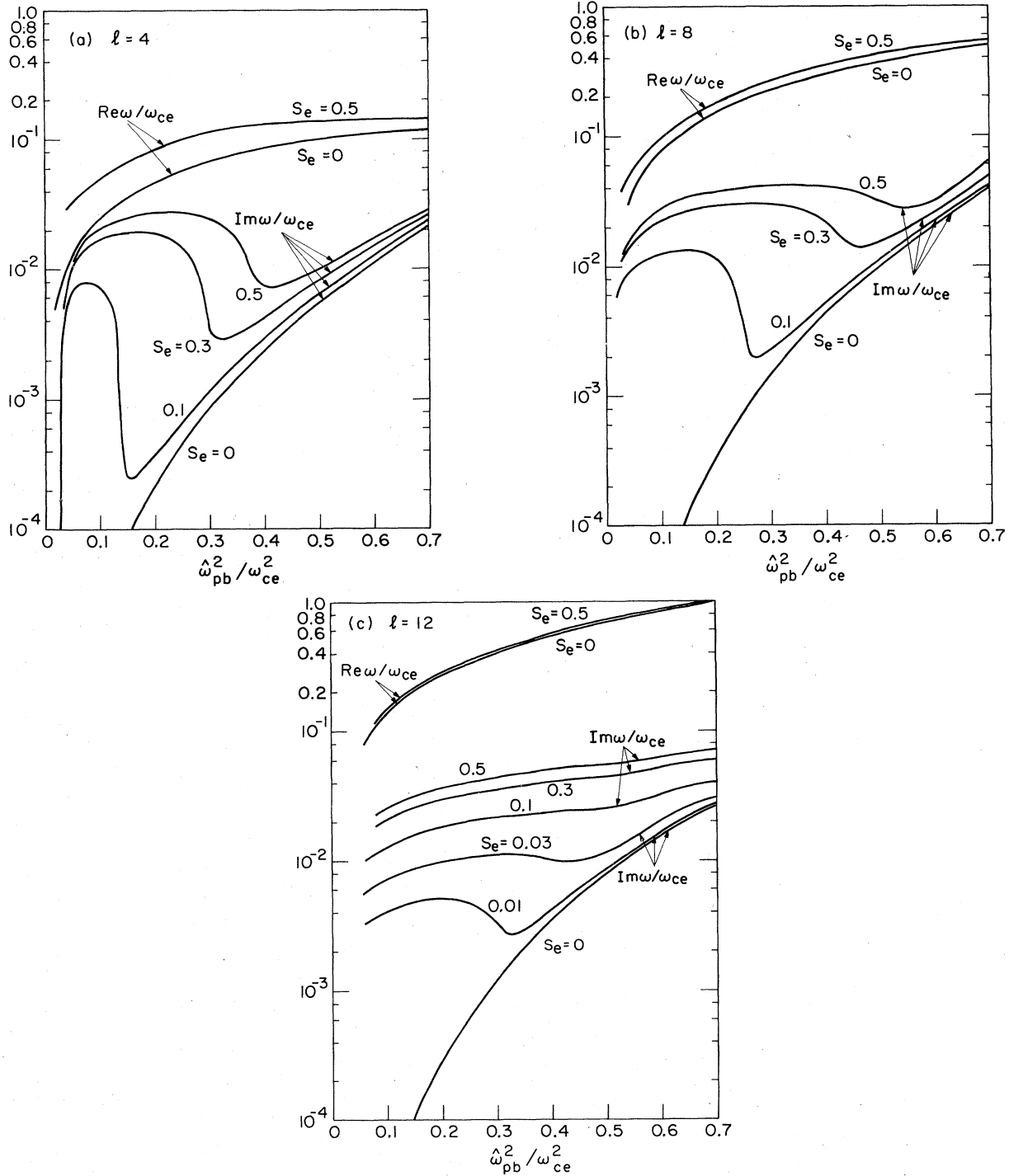

FIG. 12. Plots of normalized real frequency $(\mathrm{Re}\,\omega)/\omega_{ce}$ and growth rate $(\mathrm{Im}\,\omega)/\omega_{ce}$ vs $\hat{\omega}_{pb}^2/\omega_{ce}^2$ obtained from Eq. (48) for the high-frequency branch assuming $r_b/a = 1.2$, $r_p/a = 1.4$, and $b/a = 1.6$. Stability results are presented for several values of $s_e = \hat{\omega}_{pe}^2/\omega_{ce}^2$ ranging from $s_e = 0$ to $s_e = 0.5$, and for (a) $l = 4$, (b) $l = 8$, and (c) $l = 12$.

from Fig. 11(b), for $b/a = 2$ and $\hat{n}_e/\hat{n}_b = 0.2$, the strongest instability occurs for $r_b/a \simeq 1.5$.

VI. NUMERICAL RESULTS

In this section, we make use of the exact eigenvalue equation (48) and the related definitions in Eqs. (49)—(54) and Eqs. (19)—(21) to investigate numerically the stability properties for electrostatic perturbations about the equilibrium density profiles illustrated in Fig. 2. No *a priori* assumption is made that the anode plasma density or cathode electron density is low or that the electrons are strongly magnetized. In solving Eq. (48), we impose the boundary conditions $\delta\phi^l(r=a)=0=\delta\phi^l(r=b)$, and the anode plasma between $r=r_p$ and $r=b$ is assumed to be hydrogen plasma with

$$Z_i = 1 \quad \text{and} \quad \frac{m_e}{m_i} = \frac{1}{1836} \; . \tag{94}$$

Typical numerical results are illustrated in Figs. 12 and 13 for the choice of geometric factors

$$\frac{r_b}{a} = 1.2, \quad \frac{r_p}{a} = 1.4, \quad \frac{b}{a} = 1.6 \; , \tag{95}$$

corresponding to a moderate-aspect-ratio diode. The stability results in Fig. 12 correspond to the high-frequency (electron-driven) branch (Sec. V), whereas Fig. 13 illustrates stability behavior for the low-frequency branch (ion resonance instability)[12] in which the anode plasma ions couple strongly to the cathode electrons (Sec. IV).

Beginning with the high-frequency branch, the normalized real frequency $(\text{Re}\omega)/\omega_{ce}$ and the growth rate

$(\text{Im}\omega)/\omega_{ce}$ obtained from Eq. (48) are plotted in Fig. 12 versus normalized cathode electron density $s_b = \hat{\omega}_{pb}^2/\omega_{ce}^2$ for values of $s_e = \hat{\omega}_{pe}^2/\omega_{ce}^2$ ranging from $s_e = 0$ (no anode plasma) to $s_e = 0.5$ (dense anode plasma). The numerical plots are presented for azimuthal mode numbers $l = 4$ [Fig. 12(a)], $l = 8$ [Fig. 12(b)], and $l = 12$ [Fig. 12(c)].

For no anode plasma $(s_e = 0)$ and low-density cathode electrons $(s_b = \hat{\omega}_{pb}^2/\omega_{ce}^2 \ll 1)$, it is clear from Fig. 12 that the instability growth rate is extremely small $[(\text{Im}\omega)/\omega_{ce} < 10^{-4}$ for $s_b < 0.1]$. Moreover, for $s_b \ll 1$ and $s_e = 0$, the real oscillation frequency in Fig. 12 connects smoothly onto the analytic result [see Eq. (93) with $\hat{n}_e = 0$]

$$\frac{\text{Re}\omega}{\omega_{ce}} = \frac{\hat{\omega}_{pb}^2}{2\omega_{ce}} \left[l \left[1 - \frac{a^2}{r_b^2} \right] \right.$$
$$\left. - \frac{[1-(r_b/b)^{2l}]}{[1-(a/b)^{2l}]} [1-(a/r_b)^{2l}] \right] \; . \tag{96}$$

As the cathode electron density (s_b) is increased for $s_e = 0$, it is clear from Fig. 12 that the growth rate and real frequency increase monotonically, at least for values of $\hat{\omega}_{pb}^2/\omega_{ce}^2$ up to 0.7. In addition, $\text{Re}\omega$ and $\text{Im}\omega$ increase with mode number l for the range of l presented in Fig. 12. The $s_e = 0$ results in Fig. 12 are consistent with earlier numerical studies of electrostatic stability properties carried out for the rectangular cathode electron density profile in Ref. 1.
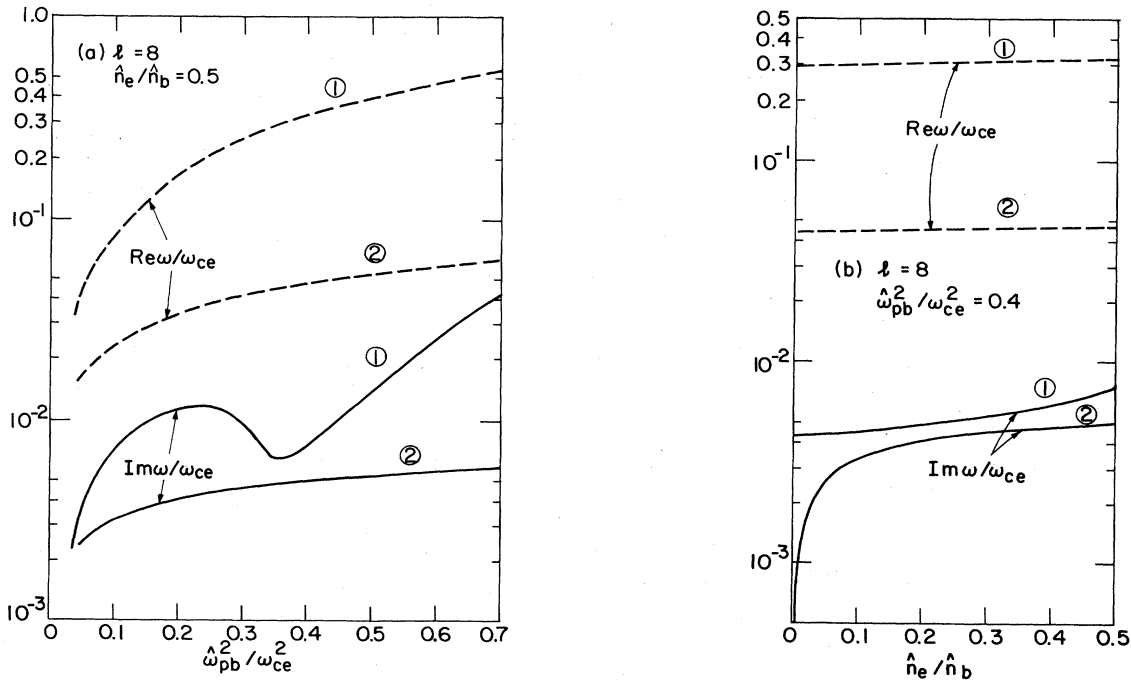

FIG. 13. Plots of normalized real frequency $(\text{Re}\omega)/\omega_{ce}$ and growth rate $(\text{Im}\omega)/\omega_{ce}$ obtained from Eq. (48) assuming $l = 8$, $r_b/a = 1.2$, $r_p/a = 1.4$, and $b/a = 1.6$. Plots are vs (a) $\hat{\omega}_{pb}^2/\omega_{ce}^2$, for $\hat{n}_e/\hat{n}_b = 0.5$, and (b) $\hat{n}_e/\hat{n}_b$, for $\hat{\omega}_{pb}^2/\omega_{ce}^2 = 0.4$. Both the high-frequency branch (labeled by 1) and the low-frequency branch (labeled by 2) are displayed.

For nonzero anode plasma density $(s_e \neq 0)$, it is clear from Fig. 12 that the instability growth rate and real oscillation frequency are enhanced relative to the $s_e = 0$ case. This is due to a coupling between the plasma electrons and the cathode electrons. Evidently, this coupling can be particularly strong in the low-density regime (Sec. V). For example, for $l = 8$ and $s_b = \hat{\omega}_{pb}^2/\omega_{ce}^2 = 0.2$ it follows from Fig. 12(b) that $(\mathrm{Im}\omega)/\omega_{ce} = 3.5 \times 10^{-4}$ for $s_e = \omega_{pe}^2/\omega_{ce}^2 = 0$, whereas $(\mathrm{Im}\omega)/\omega_{ce} = 1 \times 10^{-2}$ for $s_e = \hat{\omega}_{pe}^2/\omega_{ce}^2 = 0.1$. This corresponds to a 30-fold increase in the growth rate produced by the strong interaction of the anode electrons with the cathode electrons. As s_b and s_e are increased further, the growth rate is still enhanced relative to the $s_e = 0$ case, but not by the same large factors as in the low-density regime. For the parameters chosen in Fig. 12, we also note that the enhancement in growth rate as s_e is increased is more pronounced at larger l values, whereas the enhancement in real oscillation frequency as s_e is increased tends to be weaker at larger l values.

We now consider Fig. 13 where the numerical results obtained from Eq. (48) are presented for both the low-frequency (ion-driven) branch as well as the high-frequency (electron-driven) branch. In Fig. 13, and throughout the remainder of this paper (Figs. 14 and 15), the high-frequency and low-frequency solutions are labeled by the numbers 1 and 2, respectively. Shown in Fig. 13 are plots of the normalized real frequency $(\mathrm{Re}\omega)/\omega_{ce}$ and growth rate $(\mathrm{Im}\omega)/\omega_{ce}$ for the mode number $l = 8$ and geometric parameters specified by $r_b/a = 1.2$, $r_p/a = 1.4$, and $b/a = 1.6$ [Eq. (95)]. In Fig. 13(a), the real frequency and growth rate are plotted versus $s_b = \hat{\omega}_{pb}^2/\omega_{ce}^2$ for fixed density ratio $\hat{n}_e/\hat{n}_b = 0.5$. On the other hand, in Fig. 13(b), the real frequency and growth rate are plotted versus density ratio $\hat{n}_e/\hat{n}_b$ for a fixed value of $\hat{\omega}_{pb}^2/\omega_{ce}^2 = 0.4$. Several features of the stability behavior are evident from Fig. 13. First, the real oscillation frequency for the ion-driven branch (curve set no. 2) is about an order of magnitude lower (or somewhat less) than the real oscillation frequency for the high-frequency branch (curve set no. 1), at least for the range of parameters analyzed in Fig. 13. Second, for fixed density ratio $\hat{n}_e/\hat{n}_b = 0.5$ and increasing values of $\hat{\omega}_{pb}^2/\omega_{ce}^2$, it is clear from Fig. 13(a) that the growth rate for the ion resonance instability increases monotonically (albeit slowly), whereas the growth rate for the high-frequency branch exhibits a secondary maximum for $s_b \simeq 0.25$ (see also Fig. 12). On the other hand, for fixed value of $\hat{\omega}_{pb}^2/\omega_{ce}^2 = 0.4$ and increasing density ratio $\hat{n}_e/\hat{n}_b$, we find from Fig. 13(b) that the growth rate for the ion resonance instability increases rapidly and begins to level off at $\mathrm{Im}\omega \simeq 0.0045\omega_{ce}$ for $\hat{n}_e/\hat{n}_b \gtrsim 0.3$, whereas the growth rate for the high-frequency branch increases slowly over the entire interval $0 < \hat{n}_e/\hat{n}_b < 0.5$. Another important feature evident from Fig. 13 is that the growth rate of the ion resonance instability can be substantial. Indeed, the growth rates of the two branches are comparable over most of the parameter range analyzed in Fig. 13(b). This is a very important result, since the ions participate as an active component for the low-frequency branch (curve set No. 2), and would be expected to exhibit a strong nonlinear response to the in-

stability.

A region of strong ion resonance instability is also illustrated in Fig. 14 where the normalized real frequency $(\mathrm{Re}\omega)/\omega_{ce}$ and growth rate $(\mathrm{Im}\omega)/\omega_{ce}$ are plotted versus $s_b = \hat{\omega}_{pb}^2/\omega_{ce}^2$ for mode number $l = 8$, fixed density ratio $\hat{n}_e/\hat{n}_b = 0.5$, and diode aspect ratio increased from $a/(b-a) = 1.67$ (in Figs. 12 and 13) to $a/(b-a) = 4.76$ (in Fig. 14). For the parameter range analyzed in Fig. 14, the real frequency of the two branches differ by less than a factor of 2. On the other hand, the growth rate of the ion resonance instability (curve set no. 2) is substantially larger than the growth rate of the high-frequency branch (curve set no. 1) over a wide range of cathode electron density $(s_b \lesssim 0.4)$.

The strong dependence of instability growth rate and real oscillation frequency on diode aspect ratio was evident from the analytic studies of the two branches presented in Secs. IV and V. This is further illustrated in Fig. 15, where the normalized real frequency $(\mathrm{Re}\omega)/\omega_{ce}$ and growth rate $(\mathrm{Im}\omega)/\omega_{ce}$ obtained from Eq. (48) are plotted versus normalized diode thickness Δ defined by

$$\Delta = \frac{b-a}{a} . \tag{97}$$

As in Figs. 12—14, the relative thickness of the cathode electron layer, the vacuum region, and the anode plasma, each correspond to one-third of the total cathode-anode spacing. That is, in Fig. 15,

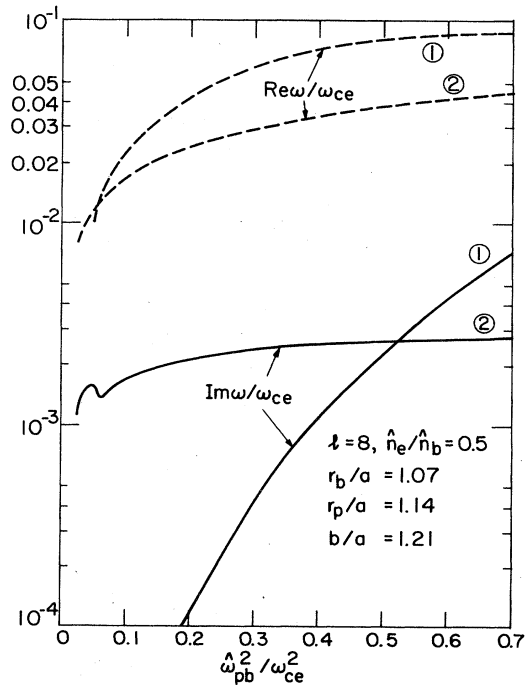$$\frac{r_b}{a} = 1 + \frac{1}{3}\Delta, \quad \frac{r_p}{a} = 1 + \frac{2}{3}\Delta . \tag{98}$$

FIG. 14. Plots of normalized real frequency $(\mathrm{Re}\omega)/\omega_{ce}$ and growth rate $(\mathrm{Im}\omega)/\omega_{ce}$ vs $\hat{\omega}_{pb}^2/\omega_{ce}^2$ obtained from Eq. (48) for $l = 8$, $\hat{n}_e/\hat{n}_b = 0.5$, $r_b/a = 1.07$, $r_p/a = 1.14$, and $b/a = 1.21$. Both the high-frequency branch (labeled by 1) and the low-frequency branch (labeled by 2) are displayed.

Moreover, $l = 8$ and fixed density ratio $\hat{n}_e / \hat{n}_b = 0.5$ are assumed in Fig. 15, with $s_b = \hat{\omega}_{pb}^2 / \omega_{ce}^2 = 0.4$ in Fig. 15(a) and $s_b = 0.7$ in Fig. 15(b). Comparing Figs. 15(a) and 15(b), it is found that the plots of the real oscillation fre-
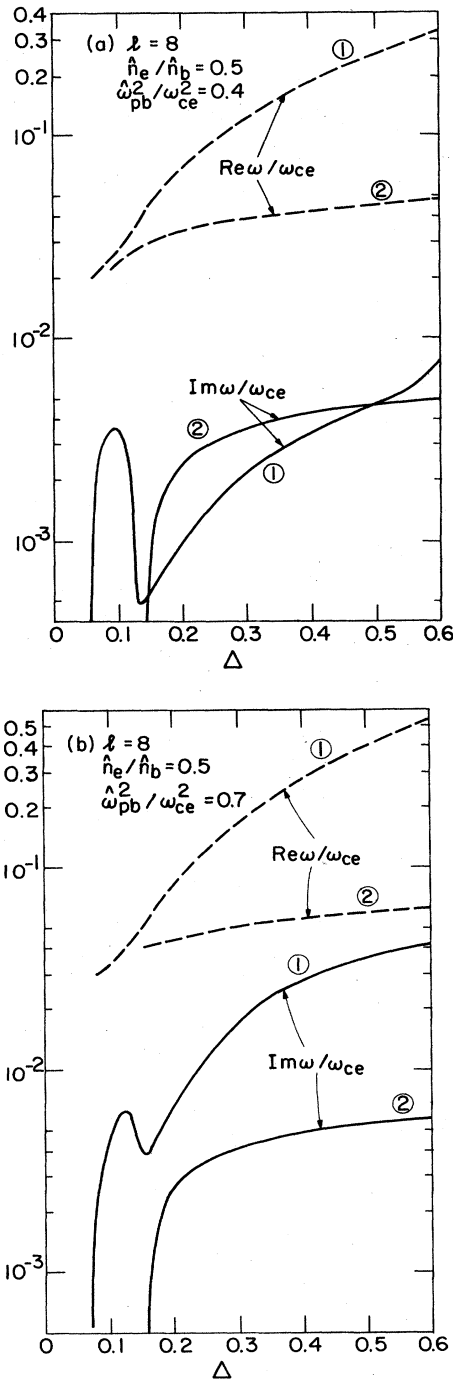

FIG. 15. Plots of normalized real frequency $(\mathrm{Re}\omega)/\omega_{ce}$ and growth rate $(\mathrm{Im}\omega)/\omega_{ce}$ vs $\Delta = (b - a)/a$ obtained from Eq. (48) for $l = 8$, $\hat{n}_e / \hat{n}_b = 0.5$, and (a) $\hat{\omega}_{pb}^2 / \omega_{ce}^2 = 0.4$, and (b) $\hat{\omega}_{pb}^2 / \omega_{ce}^2 = 0.7$. In (a) and (b) it is assumed that $(r_b - a)/a = \Delta/3$ and $(r_p - a)/a = 2\Delta/3$. Both the high-frequency branch (labeled by 1) and the low-frequency branch (labeled by 2) are displayed.

quency for both branches and the growth rate for the ion resonance instability (curve set no. 2) are relatively insensitive to increasing the cathode electron density from $s_b = \hat{\omega}_{pb}^2 / \omega_{ce}^2 = 0.4$ [Fig. 15(a)] to $\hat{\omega}_{pb}^2 / \omega_{ce}^2 = 0.7$ [Fig. 15(b)]. On the other hand, there is a significant increase in the growth rate of the high-frequency branch (curve set no. 1) as s_b is increased. In addition, for the parameter range analyzed in Fig. 15, there is an abrupt increase in the growth rate of the ion resonance instability as Δ is increased, with $\mathrm{Im}\omega$ beginning to level off at $\mathrm{Im}\omega \simeq 0.005\omega_{ce}$ for $\Delta \gtrsim 0.5$. Moreover, it is evident from Fig. 15 that the growth rate of the high-frequency branch exhibits a secondary maximum (for $\Delta \simeq 0.1$) as Δ is increased. Although the detailed physical reason for this growth enhancement (secondary maximum) is not understood at the present time, the reader will recall from the analytic studies in Sec. V that the instability growth rate of the high-frequency branch exhibits a very sensitive dependence on the geometric factors r_b/a, r_b/a, and b/a.

VII. CONCLUSIONS

In this paper we have made use of the macroscopic cold-fluid-Poisson equations to investigate collective instabilities driven by anode plasma ions and electrons in a nonrelativistic cylindrical diode with applied magnetic field $B_0 \hat{e}_z$. Following a review of equilibrium properties (Sec. II), the electrostatic eigenvalue equation is derived (Sec. III) and investigated analytically (Secs. IV and V) and numerically (Sec. VI) assuming flute perturbations with $\partial/\partial z = 0$. Particular emphasis is placed on the influence of the anode plasma on stability behavior assuming uniform cathode electron density $(\hat{n}_b)$ extending from $r = a$ to $r = r_b$, and uniform anode plasma density $(\hat{n}_e = Z_i \hat{n}_i)$ extending from $r = r_p$ to $r = b$. Depending on the cathode electron density (as measured by $s_b = \hat{\omega}_{pb}^2 / \omega_{ce}^2$), the anode plasma density (as measured by $s_e = \hat{\omega}_{pe}^2 / \omega_{ce}^2$), the diode aspect ratio, etc., it is found that there can be a strong coupling of the anode plasma to the cathode electrons, and a concomitant large influence on detailed stability behavior. In particular, the presence of the anode plasma ions introduces a new low-frequency mode (ion resonance instability) in which there is a strong coupling of the anode plasma ions to the cathode electrons (Secs. IV and VI). Moreover, the conventional high-frequency stability properties calculated for $s_e = 0$ are significantly modified by the coupling between the cathode electrons and the anode plasma electrons (Secs. V and VI). For example, for $b/a = 1.6$, $r_b/a = 1.2$, $r_p/a = 1.4$, $l = 8$, and $s_b = 0.2$, it is found that $(\mathrm{Im}\omega)/\omega_{ce} = 3.5 \times 10^{-4}$ for $s_e = 0$, whereas $(\mathrm{Im}\omega)/\omega_{ce} = 10^{-2}$ for $s_e = 0.1$, corresponding to a 30-fold increase in instability growth rate [Fig. 12(b)].

ACKNOWLEDGMENTS

[1]R. C. Davidson and K. Tsang, Phys. Rev. A 29, 488 (1984).

[2]R. C. Davidson, K. Tsang, and J. Swegle, Phys. Fluids 27, 2332 (1984).

[3]J. Swegle, Phys. Fluids 26, 1670 (1983).

[4]J. Swegle and E. Ott, Phys. Fluids 24, 1821 (1981).

[5]J. Swegle and E. Ott, Phys. Rev. Lett. 46, 929 (1981).

[6]R. C. Davidson, Phys. Fluids (to be published).

[7]J. P. VanDevender, J. P. Quintenz, R. J. Leeper, D. J. Johnson, and J. T. Crow, J. Appl. Phys. 52, 4 (1981).

[8]R. H. Levy, Phys. Fluids 8, 1288 (1965).

[9]R. J. Briggs, J. D. Daugherty, and R. H. Levy, Phys. Fluids 13, 421 (1970).

[10]O. Buneman, R. H. Levy, and L. M. Linson, J. Appl. Phys. 37, 3203 (1966).

[11]R. C. Davidson, *Theory of Nonneutral Plasmas* (Benjamin, Reading, Mass., 1974).

[12]R. H. Levy, J. D. Daugherty, and O. Buneman, Phys. Fluids 12, 2616 (1969).

[13]I. Haber and A. W. Maschke, Phys. Rev. Lett. 42, 1479 (1979).

[14]R. C. Davidson, Ref. 11, pp. 62—66.

[15]D. G. Koshkarev and P. R. Zenkevich, Part. Accel. 3, 1 (1972).

[16]R. C. Davidson and H. S. Uhm, Phys. Fluids 21, 265 (1978).

[17]R. C. Davidson and H. S. Uhm, Plasma Phys. 10, 579 (1978).

[18]H. S. Uhm and R. C. Davidson, Part. Accel. 11, 135 (1980).

[19]H. S. Uhm and R. C. Davidson, Phys. Fluids 25, 2334 (1982).

[20]R. C. Davidson, Ref. 11, pp. 41—45.

[21]C. L. Chang, E. Ott, T. Antonsen, and A. T. Drobot, Phys. Fluids 27, 2545 (1984).

[22]M. P. Desjarlais and R. N. Sudan, Bull. Am. Phys. Soc. 28, 1148 (1983).

[23]R. C. Davidson, Phys. Fluids 27, 1804 (1984).